



# Size effects in the conical indentation of an elasto-plastic solid

K. Danas<sup>a</sup>, V.S. Deshpande<sup>b</sup>, N.A. Fleck<sup>b,\*</sup>

<sup>a</sup> Laboratoire de Mécanique des Solides, C.N.R.S. UMR7649, Département de Mécanique, École Polytechnique, 91128 Palaiseau Cedex, France

<sup>b</sup> Centre for Micromechanics, Department of Engineering, University of Cambridge, Trumpington Street, Cambridge CB2 1PZ, UK

## ARTICLE INFO

### Article history:

Received 26 July 2011

Received in revised form

7 May 2012

Accepted 9 May 2012

Available online 17 May 2012

### Keywords:

Strain-gradient plasticity

Indentation

Mixed finite-element method

Material length-scales

Elastic-viscoplastic material

## ABSTRACT

The size effect in conical indentation of an elasto-plastic solid is predicted via the Fleck and Willis formulation of strain gradient plasticity (Fleck, N.A. and Willis, J.R., 2009, A mathematical basis for strain gradient plasticity theory. Part II: tensorial plastic multiplier, *J. Mech. Phys. Solids*, 57, 1045–1057). The rate-dependent formulation is implemented numerically and the full-field indentation problem is analyzed via finite element calculations, for both ideally plastic behavior and dissipative hardening. The isotropic strain-gradient theory involves three material length scales, and the relative significance of these length scales upon the degree of size effect is assessed. Indentation maps are generated to summarize the sensitivity of indentation hardness to indent size, indenter geometry and material properties (such as yield strain and strain hardening index). The finite element model is also used to evaluate the pertinence of the Johnson cavity expansion model and of the Nix–Gao model, which have been extensively used to predict size effects in indentation hardness.

© 2012 Elsevier Ltd. All rights reserved.

## 1. Introduction

There has been intense recent interest in size effects associated with plasticity on the micron scale and below (Evans and Hutchinson, 2009; Pharr et al., 2010). In part, this is due to the development of manufacturing techniques for devices on the micro- and nano-scales. And in part, this is a consequence of the development of new imaging and characterization techniques that allow for the observation of the deformation mechanisms (including dislocation motion) on the sub-micron scale.

Nano- and micro-indentation techniques (Pethica et al., 1983; Oliver and Pharr, 1992) now have the ability to measure the indenter force–displacement curves rather than relying upon post-test measurements of hardness impression. This has allowed for a more precise measurement of size effects in indentation hardness at impression depths from nanometer to micron. The hardness test remains a popular method of extracting information on the Young's modulus, strength and toughness of engineering metals, ceramics and polymers. It samples only a small surface region of the solid, and thereby has the merit that it can be used to probe the mechanical response of thin coatings in addition to that of bulk solids. However, the indentation test remains difficult to interpret, particularly when the indent depth is on a micron-scale or below (Pharr et al., 2010).

There is a growing body of experimental data to suggest that the hardness of metallic alloys increases with diminishing contact radius for indents in the micron range and below (Poole et al., 1996; Stelmashenko et al., 1993; Stelmashenko and Brown, 1996; Nix and Gao, 1998; Hutchinson, 2000; Pharr et al., 2010). It is appreciated that a number of physical

\* Corresponding author.

E-mail addresses: [kdanas@lms.polytechnique.fr](mailto:kdanas@lms.polytechnique.fr) (K. Danas), [vsd@eng.cam.ac.uk](mailto:vsd@eng.cam.ac.uk) (V.S. Deshpande), [naf1@cam.ac.uk](mailto:naf1@cam.ac.uk), [naf1@eng.cam.ac.uk](mailto:naf1@eng.cam.ac.uk) (N.A. Fleck).

mechanisms can give rise to such size effects. For example, indentation on the nano-scale may involve the prismatic punching of dislocations from the indenter tip (Ashby, 1970). This mechanism is similar to the so-called source-limited indentation mechanism as explored by Balint et al. (2006). At larger length scales, strength elevation is believed to be associated with the proliferation of geometrically necessary dislocations (GNDs) induced by plastic strain gradients imposed on the solid (Ashby, 1970; Fleck et al., 1994; Nix and Gao, 1998). The strength enhancement is attributed to the GNDs as follows: (i) increased plastic dissipation occurs by the motion of GNDs and gives rise to dissipative, isotropic hardening; and (ii) the elastic energy stored in the stress fields of the GNDs that gives rise to kinematic hardening.

Semi-analytical models have emerged in the literature (e.g. Ashby, 1970; Poole et al., 1996; Nix and Gao, 1998) to quantify the observed size effect in indentation. More recently, a number of nonlocal plasticity laws and minimum principles have been proposed to account for these size effects via full-field analytical/numerical implementations. These approaches are phenomenological in nature (Fleck et al., 1994; Fleck and Hutchinson, 1997; Forest et al., 2000; Fleck and Hutchinson, 2001; Gudmundson, 2004; Gurtin and Anand, 2005), are based upon crystal plasticity ideas (Fleck and Hutchinson, 1997; Gurtin, 2002; Borg, 2007; Danas et al., 2010) or are discrete dislocation based (Kubin et al., 1992; Van der Giessen and Needleman, 1995; Deshpande et al., 2005). Begley and Hutchinson (1998) used the Fleck and Hutchinson (1997) model to predict indentation size effects and explored the role of strain hardening as well as the significance of the different material length scales. They concluded that the stretch gradient is dominant in indentation problems. More recently, Komaragiri et al. (2008) have attempted to correlate material length scales as deduced from indentation measurements to predict the mode I fracture toughness behavior.

The Gurtin–Gudmundson phenomenological theory will be used in the present study together with the associated variational formulation of Fleck and Willis (2009b). In this approach, the tensorial plastic strain  $\varepsilon_{ij}^p$  is treated as a kinematic unknown in addition to the displacement  $u_i$ . In contrast, the earlier theory of Fleck and Hutchinson (1997) makes use only of the displacement  $u_i$  and its first and second derivatives in the virtual work statement. Both these phenomenological strain gradient plasticity theories can incorporate dissipative and kinematic hardening by decomposing the higher order stresses into dissipative and energetic parts as described in Fleck and Willis (2009b). In the present study, we implement numerically (using mixed finite element techniques) the Gurtin–Gudmundson strain gradient framework (Gudmundson, 2004) and the associated variational formulation of Fleck and Willis (2009b) in order to predict the size effect in indentation. We shall restrict our attention to only the dissipative hardening contribution, and justify this choice by considering the relative magnitude of elastic stored energy associated with GNDs to the plastic work for a beam in bending, see Fig. 1.

Consider a uniform array of edge dislocations as shown in Fig. 1 associated with pure bending of a beam of height  $h_b$ . The dislocation array produces a macroscopic plastic curvature  $\kappa^p = b/(sd)$ , where  $b$  is the magnitude of the Burger's vector, and  $d$  and  $s$  denote the spacing of dislocations in the  $x_1$  and  $x_2$  directions, respectively. All dislocations are geometrically necessary and the beam has traction-free upper and lower surfaces and no net axial forces. Evans and Hutchinson (2009) have solved this problem and show that the elastic energy  $U$  per unit volume for this dislocation structure is given by

$$U = \frac{E b^2}{1-\nu^2} \left[ 2.80 + 0.42 \frac{s}{d} \right], \quad \frac{s}{d} \geq 1, \quad (1)$$

in terms of the Young modulus  $E$  and Poisson's ratio  $\nu$ . The plastic work  $W^p$  per unit volume may be estimated as

$$W^p = M_p \kappa^p / h_b, \quad (2)$$

where the plastic bending moment per unit thickness  $M_p = \sigma_y h_b^2 / 4$  is given in terms of the yield strength  $\sigma_y$ . The ratio of stored elastic energy to the plastic work then follows as

$$\frac{U}{W^p} = \frac{4}{1-\nu^2} \left[ 2.80 + 0.42 \frac{s}{d} \right] \left( \frac{b}{h_b} \right) \frac{1}{\varepsilon_y}, \quad (3)$$

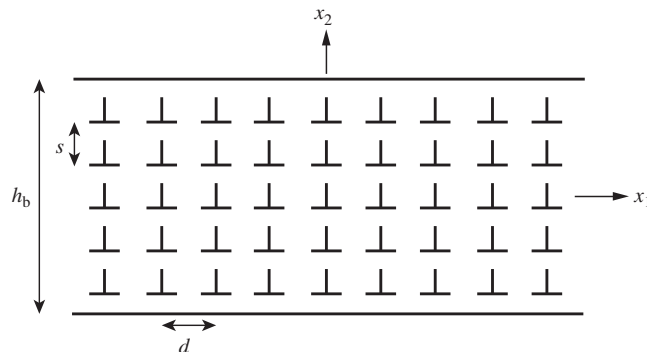


Fig. 1. A beam of height  $h_b$  contains a uniform rectangular array of dislocations. The beam undergoes pure bending due to the dislocation array.

where the yield strain is  $\varepsilon_y \equiv \sigma_y/E$ . The dissipative contribution of the GNDs outweighs their energetic contribution when  $U/W^p \ll 1$ . For example, consider a typical case with  $\nu = 0.3$ ,  $b = 0.25$  nm and  $s = d$ . Then, the dissipative contribution of the GNDs dominates the energetic part for the case

$$h_b \gg \frac{3.5}{\varepsilon_y} \text{ nm}, \quad (4)$$

i.e.  $h_b \gg 1$   $\mu\text{m}$ , for a representative yield strain of 0.35%. Thus, we conclude that the dissipative hardening assumption employed in the current study is appropriate for the interpretation of micron-scale indentation studies (some of which have been referenced above).

Our study will focus on conical indentation. This geometry is a simplification of the pyramidal Vicker indenter and of the Berkovich indenter and has the advantage that the predicted hardness is independent of indent depth for a conventional rate-independent solid in the absence of strain gradient effects. Thereby, any observed size dependence of hardness in conical indentation provides direct evidence for strain gradient strengthening. In contrast, the average strain beneath a spherical indenter increases with increasing indent depth and so more sophisticated methods are needed in order to distinguish strain gradient strengthening from strain hardening. The following dependence of hardness  $H$  in conical indentation upon indent depth  $h$  has been observed in a number of theoretical and experimental studies (Poole et al., 1996; Nix and Gao, 1998; Pharr et al., 2010):

$$\left(\frac{H}{H_0}\right)^2 = 1 + \frac{h^*}{h}, \quad (5)$$

where the length scale  $h^*$  is treated as a material property and  $H_0$  is the hardness at large indentation depths (i.e.,  $h \gg h^*$ ). Although this relation can be motivated by basic dislocation arguments, it should be regarded as a useful empirical fit to experimental data over a limited range of indent depth, as recently discussed by Pharr et al. (2010) and by Nachum et al. (2010). One of the aims of the present investigation is to explore theoretically the sensitivity of hardness to the strain hardening exponent which does not enter explicitly into the relation (5).

### 1.1. Scope of the study

Following this introduction, we present briefly the field equations and constitutive rules for an elasto-viscoplastic strain gradient solid and we then detail the assumed boundary conditions for the conical indentation problem. A finite element implementation is described, and the sensitivity of indentation response to the relative magnitude of three material length scales within the constitutive law is explored for the non-hardening case. Indentation maps are constructed in order to display the regimes of elastic response, elasto-plastic response and rigid-plastic behavior as a function of cone angle, yield strain and size of indent (in relation to the three material length scales). The role of strain hardening upon the average indentation pressure is assessed and the ability of the Tabor approximation to account for strain hardening effects is extended down to the micron-scale (where strain gradients dominate). The numerical analysis is also used to evaluate existing analytical models for indentation: the cavity expansion model and the Nix–Gao model.

## 2. The strain gradient formulation

The essential details of the Gurtin (2002)–Gudmundson (2004) strain gradient theory, along with its variational structure as introduced by Fleck and Willis (2009b), are summarized below.

*Kinematics:* The primary kinematic variables are the velocity  $\dot{u}_i$  (where the over-dot denotes time derivative) and the plastic strain-rate  $\dot{\varepsilon}_{ij}^p$ . The total strain-rate  $\dot{\varepsilon}_{ij}$  is the symmetric part of the spatial gradient of  $\dot{u}_i$  in the usual manner, and is additively decomposed into an elastic part  $\dot{\varepsilon}_{ij}^e$  and an incompressible plastic part  $\dot{\varepsilon}_{ij}^p$  according to

$$\dot{\varepsilon}_{ij} = \frac{1}{2}(\dot{u}_{i,j} + \dot{u}_{j,i}), \quad \dot{\varepsilon}_{ij} = \dot{\varepsilon}_{ij}^e + \dot{\varepsilon}_{ij}^p, \quad \dot{\varepsilon}_{ii}^p = 0. \quad (6)$$

We note in passing that the plastic strain-rate and the elastic strain-rate are each incompatible fields, but taken together the overall strain rate derives from the velocity field.

*Principle of virtual work:* Consider a solid of volume  $V$  and external surface  $S$ . Write  $q_{ij}$  as a stress-like quantity that is work conjugate to the plastic strain-rate  $\dot{\varepsilon}_{ij}^p$ ,  $\tau_{ijk}$  as a higher order stress field which is work conjugate to the gradient of the plastic strain-rate  $\dot{\varepsilon}_{ij,k}^p$  (where the subscript  $(\cdot)_i$  denotes partial derivatives with respect to the spatial coordinate  $x_i$ ), and write  $\sigma_{ij}$  as the Cauchy stress that is the work conjugate to the elastic strain rate  $\dot{\varepsilon}_{ij}^e$ .  $T_i$  and  $t_{ij}$  are the surface traction and higher order traction, work conjugate to the displacement rate  $\dot{u}_i$  and plastic strain-rates  $\dot{\varepsilon}_{ij}^p$ , respectively. Then, the principle of virtual work states that (Gudmundson, 2004; Fleck and Willis, 2009b)

$$\int_V [\sigma_{ij} \delta \dot{\varepsilon}_{ij}^e + q_{ij} \delta \dot{\varepsilon}_{ij}^p + \tau_{ijk} \delta \dot{\varepsilon}_{ij,k}^p] dV = \int_S [T_i \delta \dot{u}_i + t_{ij} \delta \dot{\varepsilon}_{ij}^p] dS, \quad (7)$$

where  $\delta(\cdot)$  denotes an arbitrary variation in  $(\cdot)$ .

Integration by parts in (7) leads to the strong form of the field equations

$$\sigma_{ij,j} = 0, \quad q_{ij} - \tau_{ijk,k} = \sigma'_{ij}, \quad \text{in } V, \quad (8)$$

with  $\sigma'_{ij}$  denoting the deviatoric Cauchy stress and  $\sigma_{ij} = \sigma_{ji}$ ,  $q_{ij} = q_{ji}$ ,  $q_{ii} = 0$ ,  $\tau_{ijk} = \tau_{jik}$  and  $\tau_{iik} = 0$ . The equilibrium statements (8) in  $V$  are complemented by equilibrium statements on the boundary, i.e.,

$$T_i = \sigma_{ij} n_j, \quad t_{ij} = \tau_{ijk} n_k, \quad \text{on } S, \quad (9)$$

where  $n_i$  is the outward unit normal to the boundary surface  $S$ .

**Constitutive relations:** In the original work of Fleck and Willis (2009a,b), the proposed constitutive models take into account internal energy storage due to both elastic straining and dislocation accumulation (Ashby, 1970) and also plastic dissipation due to dislocation motion. In the present study, we restrict attention to elasto-viscoplastic (i.e., rate-dependent) solids that store elastic strain energy and dissipate energy by plastic straining and by plastic strain gradients. The underlying physical assumption is that non-uniform plastic straining involves the motion of statistically stored and geometrically necessary dislocations. This motion gives rise to plastic dissipation and outweighs the energetic component associated with dislocation storage as argued above and as discussed by Evans and Hutchinson (2009). (The reader is referred to Fleck and Willis (2009b) and Danas et al. (2010) for a discussion of the range of constitutive behaviors that can be obtained by the use of the present strain gradient plasticity framework.)

By restricting attention to isotropic solids, the elastic energy  $U$  and the Cauchy stress  $\sigma_{ij} = \partial U / \partial \varepsilon_{ij}^e$  are expressed as

$$U(\varepsilon_{ij}^e) = \frac{E}{2(1+\nu)} \left( \varepsilon_{ij}^e \varepsilon_{ij}^e + \frac{\nu}{1-2\nu} (\varepsilon_{kk}^e)^2 \right), \quad \sigma_{ij} = \frac{E}{1+\nu} \left( \varepsilon_{ij}^e + \frac{\nu}{1-2\nu} \varepsilon_{kk}^e \delta_{ij} \right), \quad (10)$$

where  $\delta_{ij}$  are the Cartesian components of the second-order identity tensor (Kronecker delta).

In turn, the viscoplastic behavior of the solid is characterized in terms of the plastic strain-rate  $\dot{\varepsilon}_{ij}^p$  and its gradient  $\dot{\varepsilon}_{ij,k}^p$ . Upon introducing the notation (Fleck and Hutchinson, 2001)

$$\dot{\varepsilon}_{ij,k}^p \equiv \rho_{ijk} = \rho_{jik}, \quad (11)$$

we write the overall plastic strain-rate as (Smyshlyaev and Fleck, 1996; Fleck and Hutchinson, 1997, 2001; Wei and Hutchinson, 2003)

$$\dot{E}_p = \sqrt{\frac{2}{3} (\dot{\varepsilon}_{ij}^p \dot{\varepsilon}_{ij}^p + I_1^2 I_1 + 4 I_2^2 I_2 + \frac{8}{3} I_3^2 I_3)}, \quad (12)$$

in terms of three invariants  $I_1$ ,  $I_2$  and  $I_3$ , as given by

$$I_1 = \rho_{ijk}^S \rho_{ijk}^S - \frac{4}{15} \rho_{kii} \rho_{kjj}, \quad I_2 = \frac{1}{3} (\chi_{ij} \chi_{ij} + \chi_{ij} \chi_{ji}), \quad I_3 = \frac{2}{3} (\chi_{ij} \chi_{ij} - \chi_{ij} \chi_{ji}). \quad (13)$$

Here,

$$\rho_{ijk}^S = \frac{1}{3} (\rho_{ijk} + \rho_{jki} + \rho_{kij}), \quad \chi_{ij} = e_{iqr} \rho_{jrq}, \quad I_1 + I_2 + I_3 = \rho_{ijk} \rho_{ijk}. \quad (14)$$

and  $e_{ijk}$  denotes the permutation symbol. We note in passing that the first invariant  $I_1$  comprises stretch and rotation gradients, while  $I_2$  and  $I_3$  involve only rotation gradients via the curvature tensor  $\chi_{ij}$ .

The overall plastic strain-rate (12) is an isotropic measure that is homogeneous of degree one in the plastic strain-rate tensor and its first gradient. The three material length-scales  $l_i$  ( $i = 1, 2, 3$ ) are introduced for dimensional consistency in expression (12). One of the main objectives of the present study is to explore the sensitivity of any predicted size effect in indentation to the length scales  $l_i$ .

In Table 1, we introduce three particular choices  $C_1$ ,  $C_2$  and  $C_3$  for the relative magnitude of the length scales  $l_i$ . For each choice, we write the length scales  $l_i$  in terms of a single reference length scale  $l$ . Our purpose is to reveal the relative significance of each length scale  $l_i$  upon the predicted hardness.

In case  $C_1$ , the overall plastic strain-rate reduces to the form

$$\dot{E}_p = \sqrt{\frac{2}{3} (\dot{\varepsilon}_{ij}^p \dot{\varepsilon}_{ij}^p + l^2 \dot{\varepsilon}_{ij,k}^p \dot{\varepsilon}_{ij,k}^p)}, \quad (15)$$

while case  $C_2$  refers to a solid with no contributions from  $I_2$  and  $I_3$ . Case  $C_3$  corresponds to a solid such that the strain gradient dependence of  $\dot{E}_p$  only involves the invariant  $\chi_{ij} \chi_{ij}$  of the curvature tensor: this choice corresponds to the couple-stress solid as introduced by Fleck and Hutchinson (1997). It has the form

$$\dot{E}_p = \sqrt{\frac{2}{3} (\dot{\varepsilon}_{ij}^p \dot{\varepsilon}_{ij}^p + l^2 \chi_{ij} \chi_{ij})}. \quad (16)$$

**Table 1**  
Representative choices for the three length scales.

Cases	$l_1$	$l_2$	$l_3$
$C_1$	$l$	$l/2$	$\sqrt{3/8}l$
$C_2$	$l$	0	0
$C_3$	0	$l/2$	$\sqrt{5/24}l$

We proceed by considering a visco-plastic response, with a dissipation potential  $\phi$  that is power law in  $\dot{E}_p$  according to

$$\phi(\dot{\epsilon}_{ij}^p, \dot{\epsilon}_{ij,k}^p) = \int q_{ij} d\dot{\epsilon}_{ij}^p + \int \tau_{ijk} d\dot{\epsilon}_{ij,k}^p = \frac{\sigma_y \dot{\epsilon}_0}{m+1} \left( \frac{\dot{E}_p}{\dot{\epsilon}_0} \right)^{m+1} \quad (17)$$

Here,  $\dot{\epsilon}_0$  is a reference strain-rate and  $m$  is the strain-rate sensitivity parameter taking values between 1 (linear viscous) and 0 (rate-independent limit or perfect plasticity). The flow stress  $\sigma_y$  is assumed to depend upon the accumulated effective plastic strain  $E_p = \int \dot{E}_p dt$  and is here defined by

$$\sigma_y(E_p) = \sigma_0(1 + E_p/\epsilon_0)^N, \quad (18)$$

where  $\sigma_0$  is the nominal yield stress and  $\epsilon_0 = E/\sigma_0$  is the yield strain. The exponent  $N$  controls the hardening rate and takes values between 0 (non-hardening solid) and 1 (linearly hardening solid). In the following calculations, we select values of  $N$  within the practical range  $N=0$  to 0.3.

Now make use of relations (11)–(14) and of the definition (17) for the viscoplastic potential to obtain

$$q_{ij} = \frac{\partial \phi}{\partial \dot{\epsilon}_{ij}^p} = \frac{2 \sigma_y}{3 \dot{\epsilon}_0} \left( \frac{\dot{E}_p}{\dot{\epsilon}_0} \right)^{m-1} \dot{\epsilon}_{ij}^p \quad (19)$$

and

$$\tau_{ijk} = \frac{\partial \phi}{\partial \rho_{ijk}} = \frac{2 \sigma_y}{3 \dot{\epsilon}_0} \left( \frac{\dot{E}_p}{\dot{\epsilon}_0} \right)^{m-1} \left( l_1^2 R_{ijk}^{(1)} + 4 l_2^2 R_{ijk}^{(2)} + \frac{8}{3} l_3^2 R_{ijk}^{(3)} \right), \quad (20)$$

where

$$\begin{aligned} R_{ijk}^{(1)} &= \frac{1}{2} \frac{\partial I_1}{\partial \rho_{ijk}} = \rho_{ijk}^s - \frac{4}{15} \delta_{jk} \rho_{imm}, \\ R_{ijk}^{(2)} &= \frac{1}{2} \frac{\partial I_2}{\partial \rho_{ijk}} = \frac{1}{3} e_{mkj} (\chi_{mi} + \chi_{im}), \\ R_{ijk}^{(3)} &= \frac{1}{2} \frac{\partial I_3}{\partial \rho_{ijk}} = \frac{3}{5} e_{mkj} (\chi_{mi} - \chi_{im}). \end{aligned} \quad (21)$$

The above kinematical, equilibrium and constitutive relations lead to a nonlinear set of PDEs in the rate quantities  $\dot{u}_i$  and  $\dot{\epsilon}_{ij}^p$ . A solution is obtained by a mixed finite element (FEM) formulation, as described in Appendix A.

### 3. Conical indentation

We proceed by making use of the above visco-plastic strain gradient formulation in order to analyze the prototypical problem of conical indentation of a half-space. The half-space is represented by a circular cylindrical solid of height  $Z$  and radius  $R$ , both of which are much larger than the contact radius of the indenter  $a$ , see Fig. 2. The indenter is a rigid cone and its face is inclined at an angle  $\beta$  with respect to the  $r$ -axis, as shown. For simplicity, we assume complete sticking contact between the rigid indenter and the solid. This is not a severe restriction: Bower et al. (1993) have shown that the

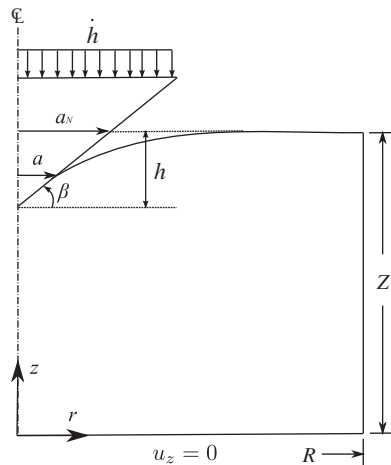


Fig. 2. Sketch of the conical indentation boundary value problem.

indentation response of a conventional visco-plastic solid is only mildly sensitive to the level of friction between indenter and solid.

In the present study, we neglect the effects of geometry changes upon the momentum balance and material rotation (i.e., we carry out a small-strain analysis) in agreement with the study of Hwang et al. (2002) who found that finite strains have only minor effects on micro-indentation hardness. Nonetheless, the contact between the rigid indenter and the specimen is based on the deformed surface of the specimen. At the current stage of deformation, the depth of the indentation is denoted by  $h$ , while  $a$  denotes the actual contact radius. Note that  $a$  differs, in general, from the nominal contact radius  $a_N \equiv h \tan \beta$  due to sink-in or pile-up, as shown schematically in Fig. 2.

An axisymmetric mixed finite element (FEM) formulation is used to predict the hardness as a function of contact radius  $a$ . At each node of the mesh, there exist five nodal unknowns: the two velocity components  $\dot{u}_r, \dot{u}_z$  and the three components of the plastic strain-rate,  $\dot{\epsilon}_{rr}^p, \dot{\epsilon}_{zz}^p$  and  $\dot{\epsilon}_{rz}^p$ . (The out-of-plane component  $\dot{\epsilon}_{\theta\theta}^p$  is readily evaluated via the incompressibility condition  $\dot{\epsilon}_{rr}^p + \dot{\epsilon}_{\theta\theta}^p + \dot{\epsilon}_{zz}^p = 0$ .) A more detailed discussion of the finite element implementation is presented in Appendix A.

The boundary condition on the contacting surface between indenter and half-space reads

$$\dot{u}_r = 0, \quad \dot{u}_z = -\dot{h}, \quad (22)$$

while the remaining part of the top-face and all the side face are traction-free. Along the bottom face ( $z=0$ ) we impose  $\dot{u}_z = 0$ . Axisymmetry about  $r=0$  is imposed through axisymmetric finite elements. Additionally, zero higher order tractions are imposed on all faces, such that  $t_{ij} = 0$ . The sensitivity of response to the choice of higher order boundary conditions is explored for a limited set of calculations in Appendix B.

The net force  $L$  on the indenter and the average contact pressure  $P$  (which is equivalent to the hardness  $H$  of the solid) are computed as

$$L = -2\pi \int_0^R T_z(r,Z) r dr \quad \text{and} \quad P = H = \frac{L}{\pi a^2}. \quad (23)$$

Here,  $T_z(r,Z)$  is the  $z$ -component of the traction vector on  $z=Z$ . Bower et al. (1993) have shown for the conventional visco-plastic solid (i.e.,  $l_1 = l_2 = l_3 = 0$ ) that the average contact pressure  $P$  can be conveniently normalized by a rate-dependent term such that

$$\bar{P}_0 = \frac{P}{[\dot{h}/(a\dot{\epsilon}_0)]^m \sigma_0}, \quad (24)$$

where  $a$  is the current actual contact radius. In the following results,  $\bar{P}_0$  will be referred to as “normalized contact pressure”. In all calculations reported below we consider the case of negligible rate sensitivity by restricting attention to  $m=0.1$ . Representative results for  $m=0.05$  and  $m=0.01$  have also been considered in order to investigate the relative importance of the strain-rate sensitivity exponent  $m$ . It has been found that a maximum quantitative difference of the order  $\sim 10\%$  is observed between the resulting normalized hardness for  $m=0.1$  and  $m=0.01$ , whereas the qualitative response remains the same for all three values  $m = 0.01, 0.05, 0.1$ . Hence, for numerical efficiency, the value  $m=0.1$  has been considered in this study.

It will be shown below that the indentation hardness of the strain-gradient solid depends upon the cone angle  $\beta$  via the non-dimensional combined parameter  $E \tan \beta / \sigma_0 (1-\nu^2)$ , as introduced originally by Johnson (1970, 1985). This non-dimensional parameter is interpreted as the ratio of the strain beneath the indenter (i.e.  $\tan \beta$ ) to the plane-strain value of yield strain (i.e.,  $\sigma_0(1-\nu^2)/E = (1-\nu^2)\epsilon_y$ , with  $\epsilon_y$  denoting the yield strain). Dimensional analysis implies that the normalized contact pressure depends upon the following non-dimensional groups:

$$\bar{P}_0 = f\left(\frac{a}{l_1}, \frac{l_2}{l_1}, \frac{l_3}{l_1}, \frac{E \tan \beta}{\sigma_0 (1-\nu^2)}, N\right). \quad (25)$$

A parametric analysis is given below for the dependence of the normalized contact pressure upon these non-dimensional groups. First, for a non-hardening solid ( $N=0$ ), the sensitivity of indentation response to the values of yield strain  $\epsilon_0 = \sigma_0/E$ , length scales  $l_1, l_2$  and  $l_3$  and the indentation angle  $\beta$  are investigated. Second, the dependence of hardness upon the strain hardening exponent  $N$  is determined. Finally, the finite element predictions are compared with the predictions for other models as taken from the literature.

#### 4. Indentation hardness for non-hardening ( $N=0$ ) gradient solids

In this section, the dependence of indentation hardness upon the independent non-dimensional groups in Eq. (25) is explored for the case of  $N=0$ . First, the accuracy of the FEM method is confirmed for the elastic case by comparison of the FEM solution with the analytical elastic solution of Sneddon (1948). The elastic FEM predictions of  $\bar{P}_0$  are plotted in Fig. 3 with an assumed  $E/\sigma_0 = 300$  so as to be consistent with the plastic results also included in the figure. Although the indent depth increases in a continuous manner, the contact radius  $a$  increases in discrete steps as given by the mesh size, and this leads to an oscillation in the estimation of the normalized contact pressure. It is clear from Fig. 3 that the mid-value of the

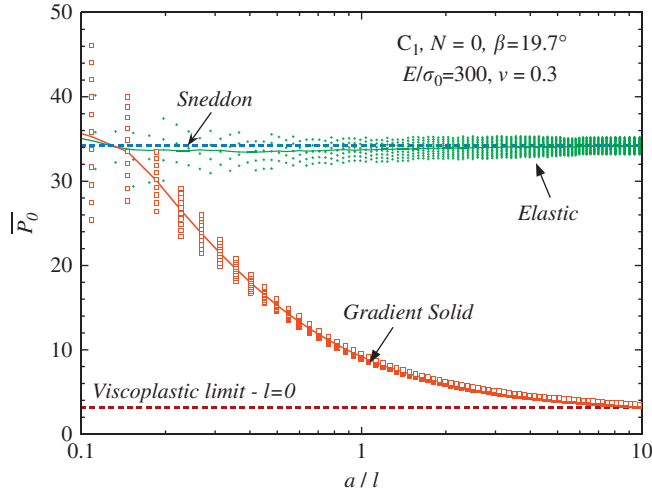


**Fig. 3.** Normalized contact pressure versus the normalized contact radius for an elastic solid, and for a strain-gradient solid of type  $C_1$  in Table 1 (with  $E/\sigma_0 = 300$ ,  $\nu = 0.3$ ). The indenter angle is  $19.7^\circ$ . For validation of the *FEM* calculations, the elastic solution of Sneddon (1948) and the rigid, ideally plastic, viscoplastic limit with no gradient effects, as provided by Bower et al. (1993), are included.

oscillations in contact pressure gives good agreement with the analytical solution: hence, we shall make use of the mid-value in all subsequent calculations.

Fig. 3 also contains a representative plot of the normalized contact pressure as a function of the normalized contact radius  $a/l$  for the elastic-ideally plastic solid ( $N=0$ ), with  $E/\sigma_0 = 300$ ,  $\nu = 0.3^1$  and  $\beta = 19.7^\circ$ . This angle corresponds to the effective cone angle for both the Berkovich and Vickers indenters. The choice  $C_1$  (of Table 1) is adopted here for the strain gradient solid.

The response of the gradient solid is initially elastic: for small values of the contact radius  $a/l \lesssim 0.2$  the normalized contact pressure in the gradient solid is almost identical to that of the Sneddon elastic solution. With increasing indentation depth, the normalized contact pressure asymptotes to the indentation hardness in the conventional viscoplastic limit  $l/a \rightarrow 0$  as predicted by Bower et al. (1993). Note that for intermediate values of the contact radius  $0.2 \leq a/l \leq 4$ , the gradient solid exhibits an increased hardness due to the development of strong plastic strain gradients beneath the indenter. The qualitative features of these calculations are in agreement with experimental evidence (Pharr et al., 2010).

We note that typically, experiments reveal that the indentation hardness increases by a factor of 2–3 when the indent radius decreases from about  $10 \mu\text{m}$  to  $0.3 \mu\text{m}$  (see, for example, the review by Pharr et al., 2010). Other indentation mechanisms, such as prismatic punching from the indenter tip, are activated at smaller contact radii. The *FEM* predictions shown in Fig. 3 extend to much higher amplifications in hardness than that observed experimentally, but we give the full range in predicted behavior in order to reveal the mathematical character of the Gurtin–Gudmundson theory: with diminishing indent size, the indentation pressure increases to that of the elastic solution. It is appreciated that the theory loses validity at such small indents and a discrete dislocation approach is more appropriate within this regime of nanoindentation.

In Fig. 4, the normalized contact pressure  $\bar{P}_0$  is plotted as a function of the normalized contact radius  $a/l$  for three different values of  $E/\sigma_0 = 10, 100, 300$  (or equivalently yield strains  $\varepsilon_0 = \sigma_0/E = 10, 1, 0.3\%$ , respectively). Parts (a), (b) and (c) of the figure correspond to the cases  $C_1, C_2$  and  $C_3$  of Table 1, respectively. In each case, the contact pressure increases with  $E/\sigma_0$ . For the choice  $E/\sigma_0 = 10$ , which corresponds to a linear elastic material with nearly no plastic strain, the contact pressure in Figs. 4(a)–(c) remains constant with increasing  $a/l$ , and no size effects are observed. This is consistent with the fact that the curves for  $E/\sigma_0 = 10$  in parts (a) to (c) are identical. When  $E/\sigma_0 = 100$ , significant plasticity develops beneath the indenter and leads to non-negligible size effects. The difference, however, between the three gradient solids  $C_1$  to  $C_3$  in parts (a) to (c) is minor. The choice  $E/\sigma_0 = 300$  leads to strong size effects in Fig. 4(a) and (b) but not in Fig. 4(c). This difference is solely attributed to the presence of a nonzero  $l_1$  in Fig. 4(a) and (b) in contrast to Fig. 4(c) where  $l_1 = 0$ . Recall that the prescription for  $\dot{\varepsilon}_p$  in the case  $C_3$  of Table 1 involves a contribution from curvature rate but neglects any contribution from the rate of stretch gradient. We conclude that stretch gradients play an important role in contributing to the size effect.

The relative importance of stretch gradient to curvature is assessed as follows. Consider a new choice for the relative magnitude of  $l_1$  compared to  $l_2 = l_3$ . Specifically, we write  $l_2 = l_3 = l$  and vary  $l_1/l$ . The dependence of  $\bar{P}_0$  upon  $l_1/l$  is given in Fig. 5 for selected sizes of indent as parameterized by  $l/a$ . In this figure, we observe that  $l_1$  becomes the dominant length

<sup>1</sup> We note that the effect of the Poisson ratio on the contact pressure is negligible and thus all results presented in the following will make use of a Poisson ratio  $\nu = 0.3$ .

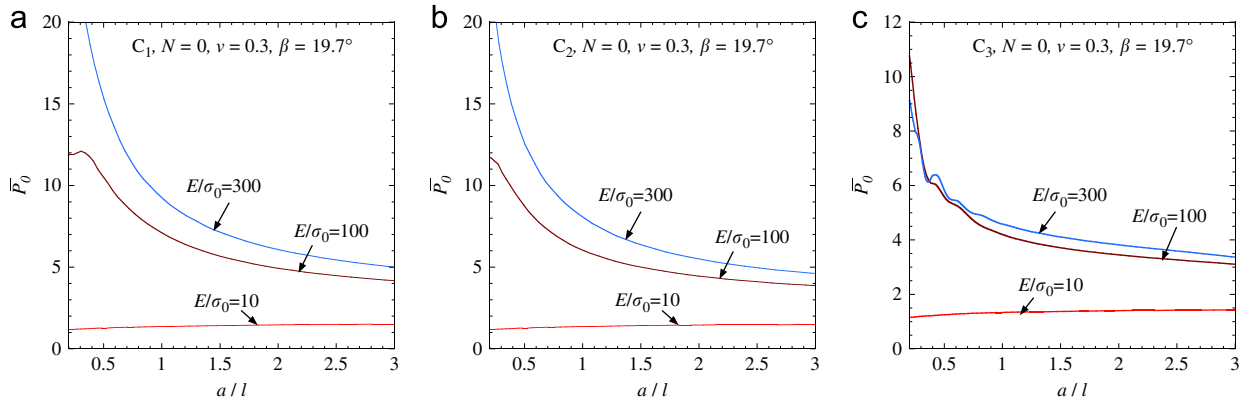


**Fig. 4.** Normalized contact pressure versus the normalized contact radius for selected values of  $E/\sigma_0 = 10, 100, 300$  for strain-gradient solids that belong to the cases (a)  $C_1$ , (b)  $C_2$  and (c)  $C_3$  as introduced in Table 1. The indenter angle is  $19.7^\circ$ .

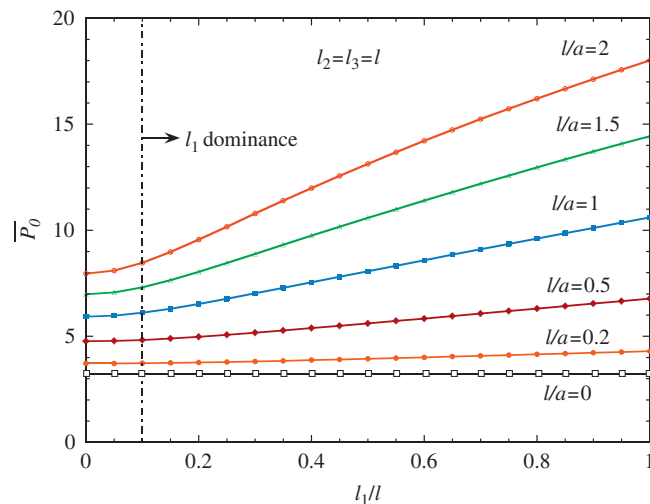


**Fig. 5.** Normalized contact pressure versus the ratio  $l_1/l$  with  $l_2 = l_3 = l$  for selected values of  $l/a$  and for  $E/\sigma_0 = 300$ ,  $\nu = 0.3$ . The indenter angle is  $19.7^\circ$ .

scale parameter when  $l_1 > 0.1l$  particularly for small contact radii  $l/a > 0.5$ . As already mentioned in connection with Fig. 4, the predicted size effects for  $l_1/l = 0$  are much weaker than those for  $l_1/l = 1$ .

#### 4.1. Construction of indentation maps

Johnson (1970) has shown that the normalized contact pressure  $\bar{P}_0$  is a function of the combined parameter  $E \tan \beta / \sigma_0 (1 - \nu^2)$  for an elastic ideally plastic solid. We proceed to develop an indentation map for the strain gradient solid (cases  $C_1$ ,  $C_2$  and  $C_3$ ) and begin by verify that the parameter  $E \tan \beta / \sigma_0 (1 - \nu^2)$  maintains its usefulness in the strain gradient setting. Fig. 6 shows a graph of normalized contact pressure as a function of the non-dimensional parameter  $E \tan \beta / \sigma_0 (1 - \nu^2)$  for two representative values of the contact radius  $l/a = 0.5, 2$  and two indentation angles,  $\beta = 19.7^\circ$  (Berkovich and Vickers indenters) and  $\beta = 47.7^\circ$  (cube corner indenter). In addition to the FEM results, the Sneddon elastic solution and the rigid plastic limit are included. The contact pressures corresponding to the two different indentation angles  $\beta = 19.7^\circ$  and  $47.7^\circ$  are in very close agreement when plotted as a function of  $E \tan \beta / \sigma_0 (1 - \nu^2)$  implying that this combined parameter captures the response for any given  $l/a$ . Thus, all subsequent numerical results employ the value  $\beta = 19.7^\circ$  and are presented in terms of  $E \tan \beta / \sigma_0 (1 - \nu^2)$ , without any loss of generality. As  $E \tan \beta / \sigma_0 (1 - \nu^2)$  is increased, the normalized pressure  $\bar{P}_0$  increases from the Sneddon solution through an elastic–plastic regime and finally asymptotes to a plateau value which is labeled the rigid plastic asymptote. It has been argued by Johnson (1970) and Wei and Hutchinson (2003) that the deformation mode switches from one of radial displacements akin to the cavity expansion mode in the elastic–plastic regime, to a surface mode in the rigid–plastic regime. We shall show below that the displacement field beneath the indenter bears little resemblance to a spherical mode and there is no switch in mode with increasing  $E \tan \beta / \sigma_0 (1 - \nu^2)$ .

Fig. 7 shows plots of normalized contact pressure versus  $E \tan \beta / \sigma_0 (1 - \nu^2)$  for the three gradient solids  $C_1$  to  $C_3$  as introduced in Table 1. The values  $l/a = 0.05, 0.25, 0.5, 1, 2$  are used to investigate the size effect for each case. For each of

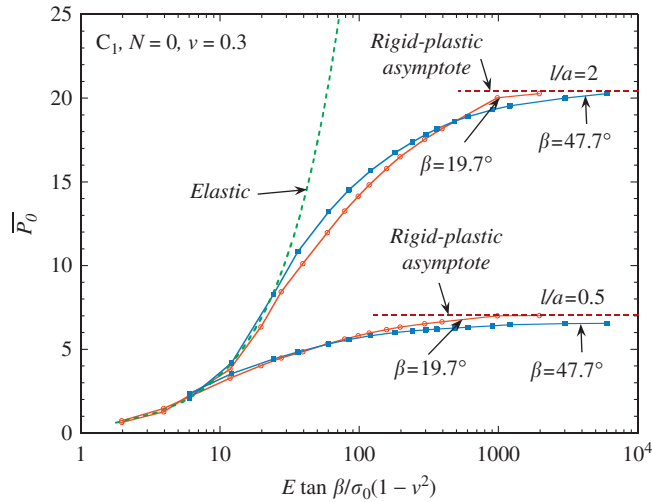


**Fig. 6.** Normalized contact pressure versus the non-dimensional strain measure  $E \tan \beta / \sigma_0 (1 - \nu^2)$  for two indenter angles  $\beta = 19.7^\circ, 47.7^\circ$  and two representative length scales  $l/a = 0.5, 2$ . The elastic Sneddon (1948) solution is included. The rigid-plastic limit is extracted by interpolation of the existing FEM estimates to high values of  $E \tan \beta / \sigma_0 (1 - \nu^2)$ .

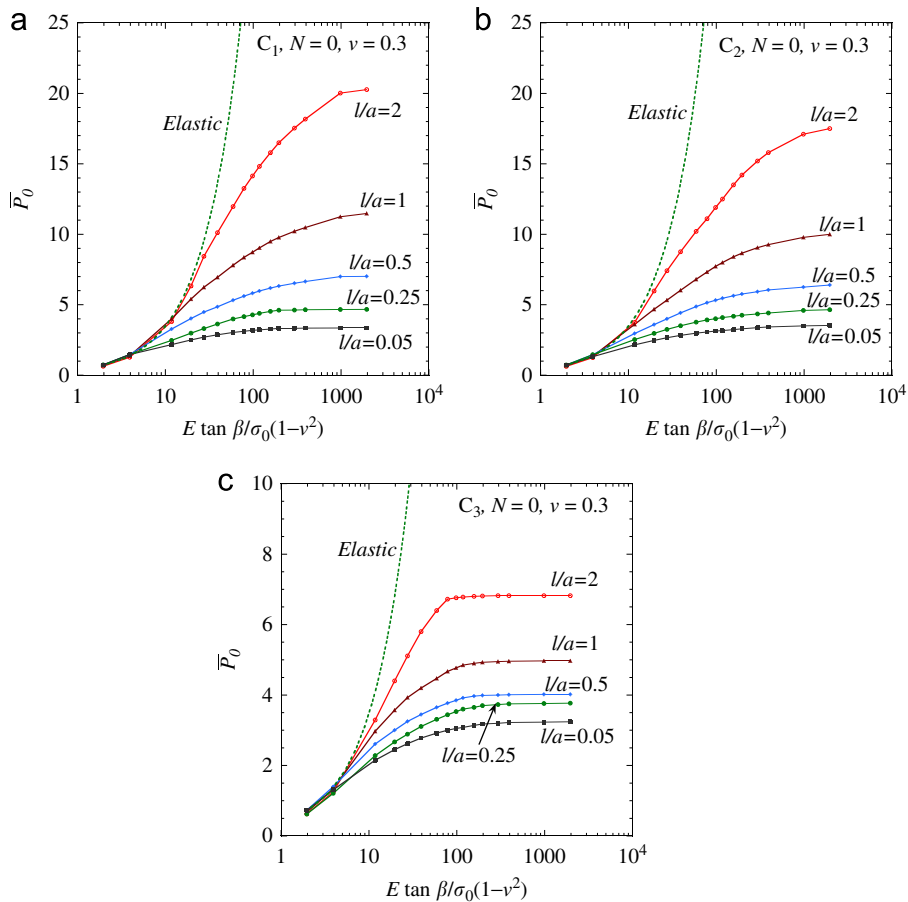


**Fig. 7.** Normalized contact pressure versus the non-dimensional strain measure  $E \tan \beta / \sigma_0 (1 - \nu^2)$  for selected values of  $l/a$ . (a) Case C<sub>1</sub>, (b) C<sub>2</sub> and (c) C<sub>3</sub>. The elastic Sneddon (1948) solution is included in each case.

the three cases C<sub>1</sub> to C<sub>3</sub>, the contact pressure increases with increasing  $E \tan \beta / \sigma_0 (1 - \nu^2)$  and with increasing  $l/a$ . As already discussed in connection with Fig. 4, the length scale  $l_1$  dominates the strain gradient contribution to strength with a much milder contribution from plastic curvature. Consequently, cases C<sub>1</sub> and C<sub>2</sub> (in Fig. 7(a) and (b), respectively) give rise to

comparable and large size effects, whereas case  $C_3$  (for which  $l_1 = 0$ , see Fig. 7(c)) predicts a smaller size effect. Upon noting that the results for case  $C_2$  are comparable to those for case  $C_1$ , our subsequent attention will be focussed upon cases  $C_1$  and  $C_3$ .

Recall from Fig. 6 that three regimes of indentation mechanism exist, depending upon the value of  $E \tan \beta / \sigma_0(1-\nu^2)$  and of  $l/a$ : (i) an elastic regime where the analytical Sneddon solution is dominant, (ii) an elasto-plastic regime where elasticity and plasticity are equally important in dictating the indentation hardness and (iii) a rigid-plastic regime where the solid exhibits significant plastic straining and elasticity is of minor importance. It is instructive to portray the regimes of dominance of each mechanism in the map of Fig. 8 by making use of the results in Fig. 7. The map takes as axes  $l/a$  and  $E \tan \beta / \sigma_0(1-\nu^2)$ , and displays the boundaries between regimes. The gradient solids  $C_1$  and  $C_2$  (with a nonzero  $l_1$ ) exhibit very similar regimes of dominance: as  $l/a$  increases both the elastic and the elasto-plastic regions extend to higher values of  $E \tan \beta / \sigma_0(1-\nu^2)$ . On the other hand, when  $l_1 = 0$  (i.e., case  $C_3$ ) the elasto-plastic regime shrinks with increasing  $l/a$ .

The map in Fig. 8 is re-plotted in Fig. 9(a) for the choice  $C_1$  and in Fig. 9(b) for the choice  $C_3$ , and now normalized contact pressure contours have been added as dashed lines. Note that the contact pressure contour lines exhibit asymptotes either at large  $l/a$  (elastic regime) or at large  $E \tan \beta / \sigma_0(1-\nu^2)$  (rigid-plastic regime). These maps can be read in a twofold fashion: (i) fix the material properties and indenter geometry by fixing  $E \tan \beta / \sigma_0(1-\nu^2)$ . Then, vary the contact size by varying  $l/a$ ; or (ii) fix  $l/a$  and vary  $E \tan \beta / \sigma_0(1-\nu^2)$ . For instance, the normalized contact pressure in a  $C_3$  solid (Fig. 9(b)) for an indenter with size  $l/a = 1$  increases with  $E \tan \beta / \sigma_0(1-\nu^2)$  but does not exceed a value of 5. On the other

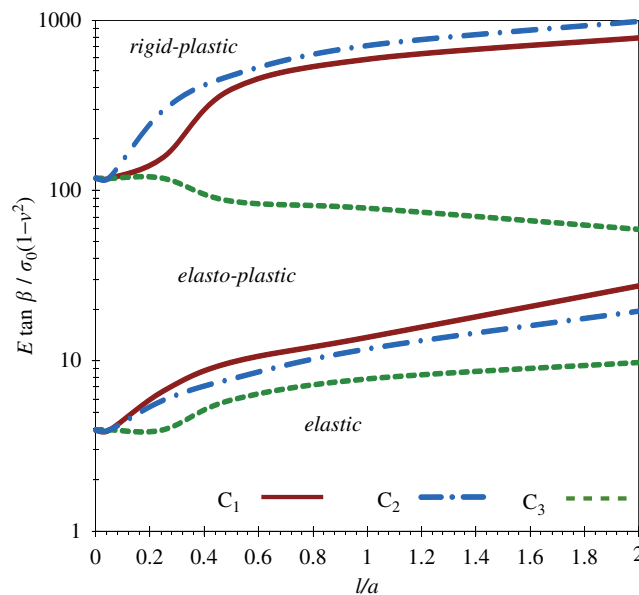


Fig. 8. Regimes of indentation mechanisms for conical indentation of the strain gradient solids as described by the cases  $C_1$ ,  $C_2$  and  $C_3$  of Table 1.

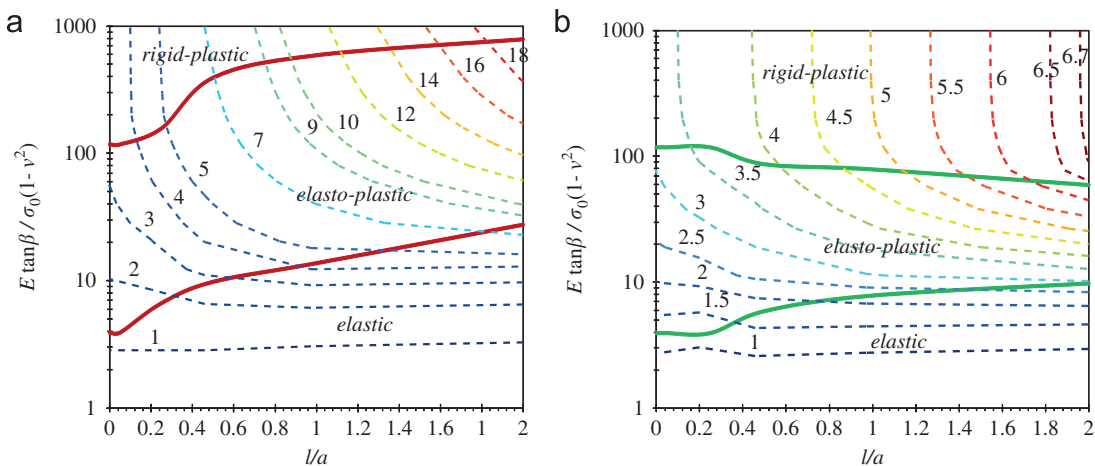


Fig. 9. Maps of conical indentation for the strain gradient solid of type (a)  $C_1$  and (b)  $C_3$ , showing regimes of deformation mechanisms. Contours of normalized contact pressure (dotted lines) are included.

hand, the normalized contact pressure for  $E\alpha/\sigma_0(1-\nu^2) = 10$  does not exceed 3 for any value of  $l/a$ . As already discussed in the context of Fig. 7, a much larger size effect is exhibited by solid  $C_1$  (where stretch gradient strengthening occurs) than that exhibited by solid  $C_3$  (where stretch gradient strengthening is absent).

4.2. Contour plots of effective plastic strain

It has been noted by Idiart et al. (2009) and Niordson and Hutchinson (submitted for publication) that strain gradient plasticity theories which involve the plastic strain as an independent kinematic quantity have the following surprising feature: they predict that continued plastic flow can occur when the Mises stress is small or even zero when large plastic gradients are present. We proceed to demonstrate that this feature of unloading of the Mises stress in the presence of continued plastic flow occurs not only in the relatively simple situations of pure bending and constrained compression as analyzed by Idiart et al. (2009) and Niordson and Hutchinson (submitted for publication), respectively, but also in the conical indentation problem as analyzed here. Contours of the Mises stress  $\sigma_e = \sqrt{3 \sigma'_{ij} \sigma'_{ij}/2}$  and of the effective plastic strain  $\epsilon_e^p = \int \sqrt{2 \dot{\epsilon}_{ij}^p \dot{\epsilon}_{ij}^p}/3 dt$  immediately below the indenter are plotted in Fig. 10 for an effective indenter angle  $\beta = 19.7^\circ$  and a non-hardening gradient solid ( $N = 0$ ) of type  $C_1$  of Table 1. (Similar observations can also be made for the cases  $C_2$  and  $C_3$  but are not shown here for the sake of brevity). Results are included for increasing indentation depth, i.e. increasing  $a/l$ . It is apparent that as  $a/l$  increases (contours from left to right),  $\sigma_e$  in Fig. 10(a) decreases over a significant region under the indenter whereas  $\epsilon_e^p$  in Fig. 10(b) increases. We anticipate that with continued loading  $\sigma_e$  will approach zero over a large part of the plastically deformed domain, as demonstrated by Idiart et al. (2009) for the case of pure bending.

This feature of strain gradient plasticity theory poses no mathematical problems in the tensor version employed here, i.e. the problem remains well-posed with positive plastic work even if  $\sigma_e \rightarrow 0$  while continued plastic flow occurs. However, it is as yet unclear whether this prediction that plastic flow can occur when the Mises stress is small or even zero is physically realistic. This remains an open research question.

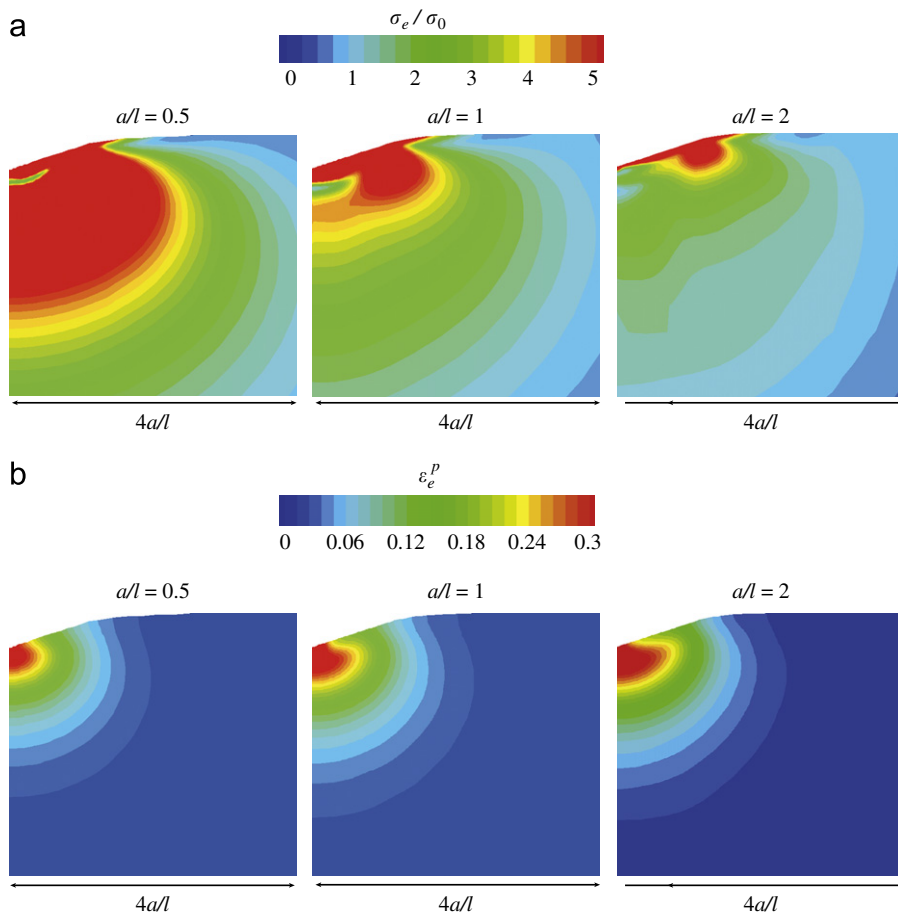


Fig. 10. Contours of (a) Mises stress  $\sigma_e$  and (b) Mises plastic strain  $\epsilon_e^p$  for three indentation depths, for a gradient solid of type  $C_1$  (of Table 1) with  $E/\sigma_0 = 300$ .

## 5. Indentation hardness for hardening gradient solids

We extend the study of indentation hardness to solids that harden according to the law (18) and for a hardening exponent  $N$  in the range of 0 to 0.3 and assess the accuracy of the Tabor (1948, 1951) approximation in the context of micro-indentation. Tabor showed that the Vickers hardness of a conventional, strain hardening solid is three times that of the material flow strength at a representative level of strain beneath the indenter, due to the effects of plastic constraint. Johnson (1985) extended this scaling law to the case of conical indentation, and argued that the representative strain is related to the cone angle according to  $\varepsilon_{rep} = 0.2 \tan \beta$ . Consequently, for the choice of hardening law (18), the Tabor approximation gives  $P = 3\sigma_{rep}$  where

$$\sigma_{rep} = \sigma_0 \left[ 1 + \frac{\varepsilon_{rep}}{\varepsilon_0} \right]^N, \quad \varepsilon_{rep} = 0.2 \tan \beta. \quad (26)$$

This approximation pertains to conventional plasticity and large values of  $E/\sigma_0$  (or small yield strains), i.e., when elasticity effects are negligible. In this regime, a number of studies have confirmed that  $P = 3\sigma_{rep}$  with  $P$  reasonably independent of the value for  $N$ , provided  $N$  is in the practical range of 0 to 0.3.

The analysis of Tabor and of Johnson neglects the contribution to hardness from material rate dependence. This can be included in the indentation analysis by introducing the notion of a representative strain rate of  $\dot{h}/a$  beneath the indenter (Bower et al., 1993). The normalized contact pressure, as defined in (24), now becomes

$$\bar{P}_T = \frac{P}{[h/(a\dot{\varepsilon}_0)]^m \sigma_{rep}}. \quad (27)$$

Thus,  $\bar{P}_T$  attempts to include the effect of strain hardening whereas  $\bar{P}_0$  neglects any contribution from strain hardening. It remains to investigate whether the above-mentioned Tabor approximation prevails down to the micron-scale, even though there is no particular theoretical reasoning for this to be the case. To help make the assessment, we plot in Fig. 11 the normalized contact pressure curves as a function of the normalized contact radius  $a/l$  for a gradient solid of type  $C_1$  (of Table 1) and  $N$  in the range 0–0.3. Fig. 11(a), (c), and (e) gives values for  $\bar{P}_0$  for  $E/\sigma_0 = 100, 300$ , and 1000, respectively, and these plots demonstrate the contribution from strain hardening to the indentation pressure. As discussed previously, the initial response of the gradient solid is purely elastic at small values of indentation depth  $a/l$ . The range of dominance of the elastic solution is sensitive to the yield strain, as parameterized by  $E/\sigma_0$ . For low values of  $E/\sigma_0$  (see for example Fig. 11(a)) the elastic solution dominates up to relatively large indentation depths, i.e.  $a/l \sim 0.4$ , whereas its dominance diminishes with increasing  $E/\sigma_0$  as observed in Fig. 11(c) and (e). At increased plastic straining,  $\bar{P}_0$  decreases to the indentation hardness in the conventional, rigid-plastic limit (i.e.  $l/a = 0$ ). This asymptote is a strong function of the hardening exponent  $N$ ; likewise, the indentation hardness at intermediate length scales depends strongly upon  $N$ .

Fig. 11(b), (d), and (f) shows the contact pressure normalized according to the Tabor approximation,  $\bar{P}_T$ , as a function of the normalized contact radius  $a/l$  for a gradient solid of type  $C_1$  (Table 1) and selected values of  $N$  in the range 0–0.3. For moderate and large values of  $E/\sigma_0$  (see Fig. 11(d) and (f)), the  $\bar{P}_T$  curves coalesce to a single curve for  $a/l > 1$  and are thereby independent of the value for  $N$ . Also,  $\bar{P}_T$  asymptotes to the Tabor value of 3 at  $l/a = 0$ . In contrast, elasticity effects dominate for the choice  $E/\sigma_0 = 100$ , see Fig. 11(b).

In similar manner, Fig. 12 shows contact pressure curves as a function of the normalized contact radius  $a/l$  for a gradient solid of type  $C_3$  of Table 1 (i.e.,  $l_1 = 0$ ) and  $N$  in the range 0–0.3. An important difference between Figs. 12(a), (c), and (e) and 11(a), (c), and (e) is that the elasticity effects at small  $a/l$  reduce significantly when  $l_1 = 0$ . This in turn leads to qualitatively different hardness estimates between the cases  $C_3$  and  $C_1$ . The Tabor approximation has a larger range of validity for the solid  $C_3$  than for the solid  $C_1$  (as seen in Fig. 12(b), (d) and (f)), i.e., it holds for smaller values of  $a/l$ .

The validity of the Tabor approximation for solids  $C_1$  and  $C_3$  of Table 1 is summarized in the form of a map with axes  $l/a$  and  $E \tan \beta / \sigma_0 (1 - \nu^2)$ , see Fig. 13. The part of the map above the dashed lines (for the case  $C_1$ ) and the dashed-dotted lines (for the case  $C_3$ ) defines the regime of validity of the Tabor approximation. As already noted in the two previous figures, the Tabor approximation exhibits a larger range of validity for the case  $C_3$  than for the case  $C_1$ .

## 6. Evaluation of existing indentation models

In this section we evaluate previous analytical models that have been proposed for the indentation hardness of solids at the micro- and macro-scales. First, we analyze the models of Johnson (1970) and Wei and Hutchinson (2003) (see also Hill, 1950); these authors predict indentation hardness from the known analytical solution for the expansion pressure of a cavity in an infinite solid. This model is compared with the numerical *FEM* results of the current study for a non-hardening gradient solid. Second, the present *FEM* strain gradient plasticity formulation is used to reproduce the hardness trends as analyzed by Nix and Gao (1998). Finally, the link between the present *FEM* model and that of Begley and Hutchinson (1998) is discussed by comparison with experiments.

### 6.1. Cavity expansion model versus *FEM* model

Johnson (1970) used the solution to the cavity expansion problem as an approximation to the indentation hardness. The merit of this approach lies in the fact that the spherical void expansion solution constitutes a one-dimensional problem

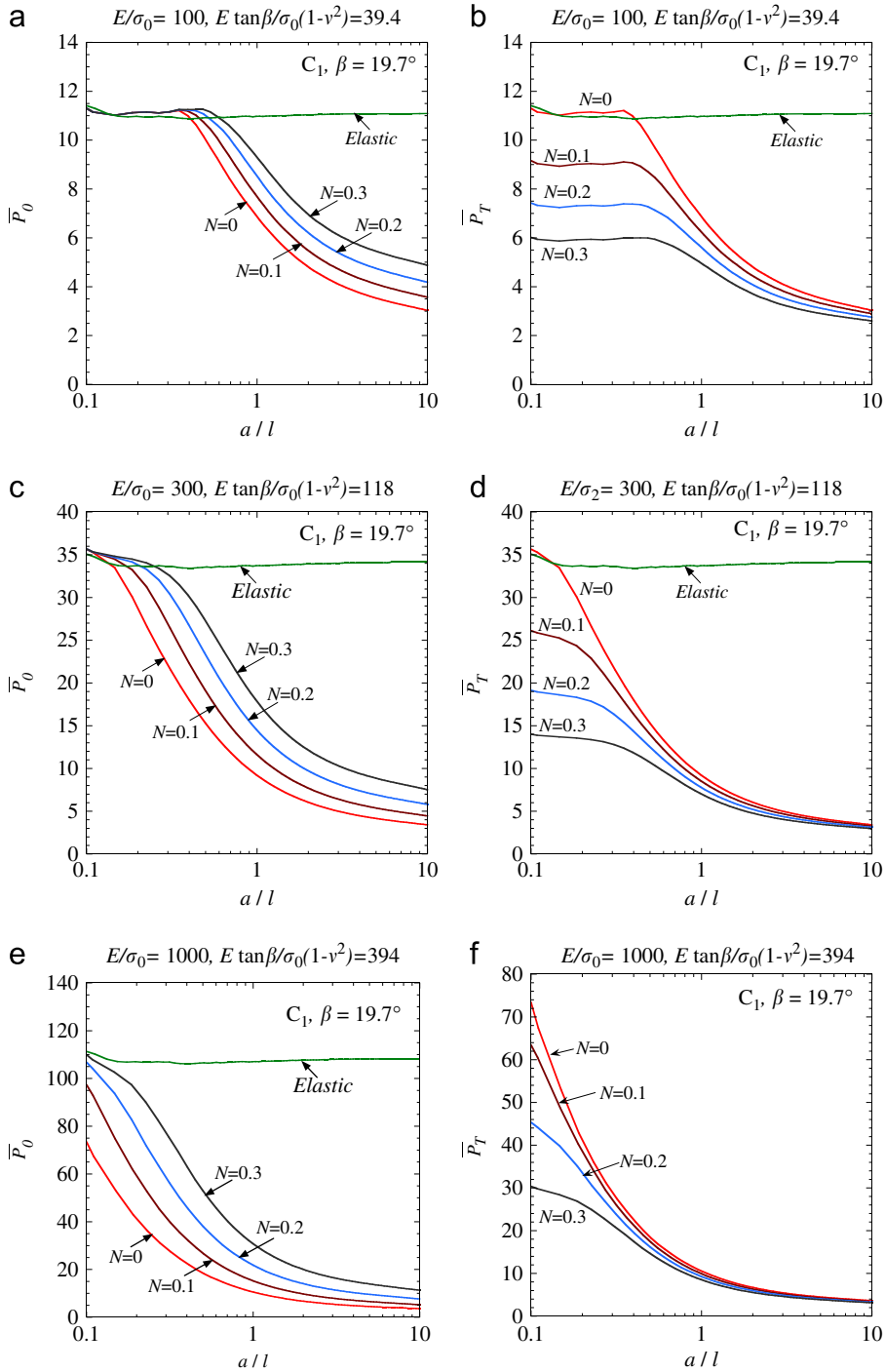


**Fig. 11.** The indentation pressure versus normalized contact radius  $a/l$  for the case  $C_1$  with (a) and (b)  $E/\sigma_0 = 100$ , (c) and (d)  $E/\sigma_0 = 300$ , (e) and (f)  $E/\sigma_0 = 1000$ . Parts (a), (c) and (e) show the effect of the exponent  $N$  on the normalized contact pressure  $\bar{P}_0$  whereas parts (b), (d) and (f) further normalize the contact pressure  $\bar{P}_T$  by making use of the reference strain  $\epsilon_{eff}$  approximation as proposed by Tabor (1951) in the context of large-scale plasticity.

(the displacement rate is only a function of the radial coordinate) and hence can be found analytically in the context of conventional elasto-(visco)plasticity as given by Hill (1950). Johnson assumed that a hemispherical core of radius  $a$  (equal to the contact radius) exists beneath the indenter contact such that the solid is in a state of uniform hydrostatic pressure,  $P_{sph} = H$ , where  $H$  is the hardness. The elastic-plastic field outside the core is represented by the field surrounding an expanding spherical cavity: the representative spherical void has expanded by  $\Delta V_{sph}$  to its current volume  $V_{sph} = 4\pi a^3/3$  by the action of an internal pressure  $P_{sph}$ . However, it remains to stipulate  $\Delta V_{sph}$  in terms of indentation geometry.

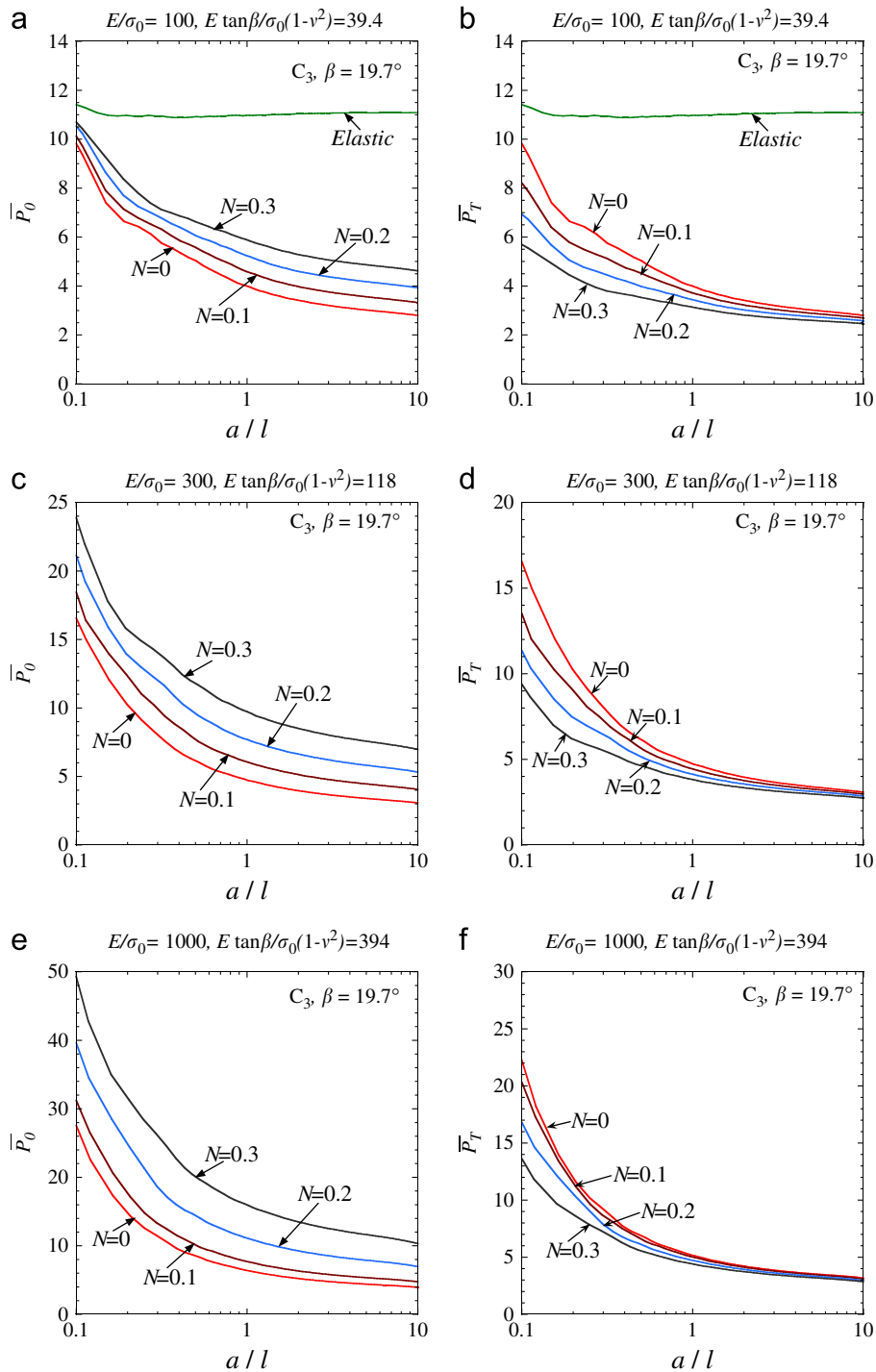


**Fig. 12.** The indentation pressure versus normalized contact radius  $a/l$  for the case  $C_3$  with (a) and (b)  $E/\sigma_0 = 100$ , (c) and (d)  $E/\sigma_0 = 300$ , (e) and (f)  $E/\sigma_0 = 1000$ . Parts (a), (c) and (e) show the effect of the exponent  $N$  on the normalized contact pressure  $\bar{P}_0$  whereas parts (b), (d) and (f) further normalize the contact pressure to  $\bar{P}_T$  by making use of the reference strain  $\epsilon_{rep}$  approximation as proposed by Tabor (1951) in the context of large-scale plasticity.

One approach followed by Wei and Hutchinson (2003) is to equate the volume of the indent with  $\Delta V_{sph}/2$  to give

$$\frac{\Delta V_{sph}}{V_{sph}} = \frac{\tan \beta}{2}. \quad (28)$$

The accuracy of this approach can be assessed as follows. The void expansion  $\Delta V_{sph}$  can be related to the infinitesimal radial displacement  $u_r$  of its surface such that  $\Delta V_{sph} = 4\pi a^2 u_r$ . Consequently, after use of approximation (28)

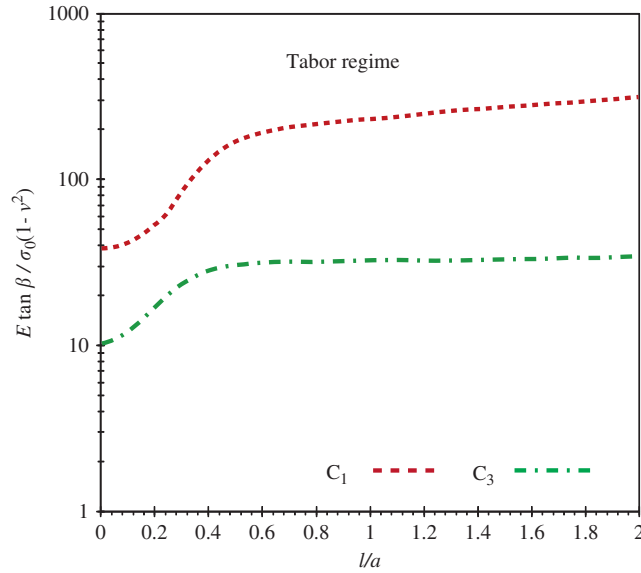


Fig. 13. The regime of validity of the Tabor approximation for conical indentation of a strain gradient solid, of type C<sub>1</sub> or C<sub>3</sub>, as defined in Table 1.

we find that

$$\frac{u_r}{a} = \frac{1}{3} \frac{\Delta V_{sph}}{V_{sph}} = \frac{\tan \beta}{6}. \tag{29}$$

We proceed to compare this with the Sneddon (1948) elastic indentation solution which predicts that the conical indentation pressure is given as

$$P_{Sneddon} = \frac{E}{1-\nu^2} \frac{\tan \beta}{2}. \tag{30}$$

On the other hand, the pressure obtained by the solution of the spherical expansion of a void in an infinite (linear) elastic medium together with the use of (29) is

$$P_{sph} = \frac{2E}{1+\nu} \frac{u_r}{a} = \frac{E}{1+\nu} \frac{\tan \beta}{3} = \frac{2(1-\nu)}{3} P_{Sneddon}. \tag{31}$$

This demonstrates that hypothesis (28) leads to an underestimation of the indentation pressure as given by the Sneddon solution in the purely elastic case. Motivated by this straightforward observation, one could prescribe

$$\frac{\Delta V_{sph}}{3V_{sph}} = \frac{u_r}{a} = \frac{\tan \beta}{4(1-\nu)}, \tag{32}$$

in order to bring the cavity expansion model into alignment with the Sneddon solution for elastic indentation. The question remains, however, whether the spherical void expansion model is an accurate approximation in the context of (micro-)indentation hardness of gradient solids.

We first solve the problem of cavity expansion in a infinite strain gradient solid (the radius of the region analyzed is 100 times the initial radius *a* of the expanding cavity). This was done by writing a one-dimensional finite element code to solve for the radial displacement and radial plastic strain in terms of radius *r*, by suitable modification of the axisymmetric finite element code. Note that in this problem, the only relevant length scale is *l*<sub>1</sub> or equivalently the single length-scale version corresponding to the solid C<sub>1</sub> (or C<sub>1</sub> ≡ C<sub>2</sub>) of Table 1. Fig. 14 shows normalized void pressure<sup>2</sup>,  $\bar{P}_0 \equiv P_{sph}/(\sigma_0(\dot{a}/(a\dot{\epsilon}_0))^m)$  curves as a function of  $\Delta V_{sph}/V_{sph}$  (lower primary *x*-axis) and *u<sub>r</sub>*/*a* (upper secondary *x*-axis) for selected values of *l/a* and for *E*/ $\sigma_0$  = 300, *N* = 0. The values of the normalized void pressure corresponding to the two approximations introduced in relations (28) and (32) can be extracted from the intersection of the dashed-dotted vertical lines with the pressure curve for any given *l/a*. As observed in Fig. 14, relation (28) leads to lower values of the normalized pressure than that of (32).

The procedure described above for the construction of Fig. 14 was repeated in order to construct a map in Fig. 15 for the case C<sub>1</sub> and *N* = 0, showing normalized contact pressure  $\bar{P}_0$  versus the strain measure *E tan β* /  $\sigma_0(1 - \nu^2)$ . Part (a) of the figure assumes *l/a* = 0.05, whereas part (b) assumes *l/a* = 1. Fig. 15 includes the full finite element predictions of indentation hardness for the elastic, ideally plastic strain-gradient solid, and also the Sneddon elastic solution for conical indentation.

<sup>2</sup> Here, the symbol  $\bar{P}_0$  is used since the void pressure estimates are directly translated to indentation hardness.

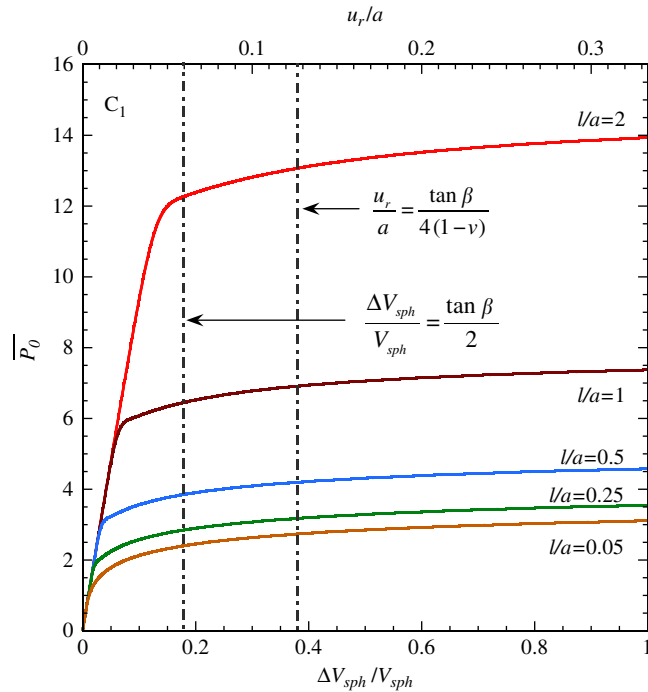


**Fig. 14.** Normalized internal void pressure versus void expansion  $\Delta V_{sph}/V_{sph} = 3u_r/a$ , according to the spherical expansion solution. All curves correspond to the  $C_1$  case with  $E/\sigma_0 = 300$ .

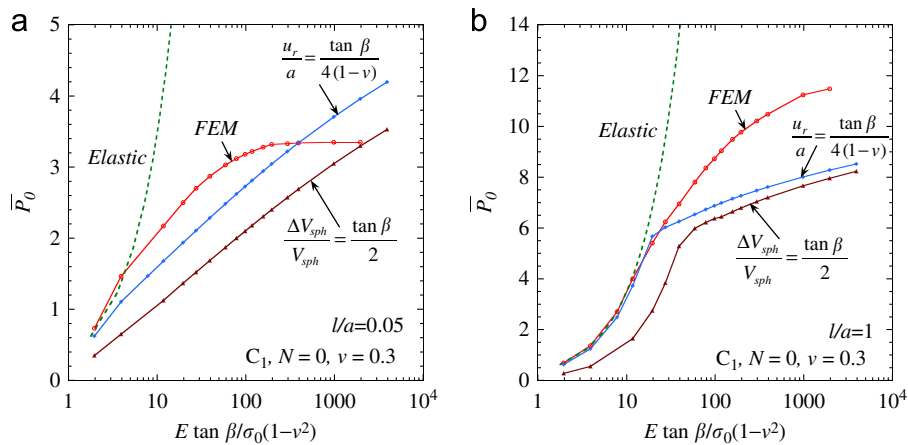


**Fig. 15.** Normalized contact pressure versus the non-dimensional strain  $E \tan \beta / \sigma_0(1-\nu^2)$  for (a)  $l/a = 0.05$  and (b)  $l/a = 1$ . All curves correspond to the case  $C_1$ . Predictions of the full-field *FEM* solution and the cavity expansion approximation based on two choices of  $\Delta V_{sph}/V_{sph}$  are included.

The choice  $l/a = 0.05$  is used in order to compare the *FEM* indentation hardness predictions with the void expansion solutions in the case corresponding to nearly conventional plasticity, while the second value  $l/a = 1$  is within the regime of micro-indentation. Neither of the approximations proposed in (28) and (32) are able to predict accurately the indentation pressure of a solid that exhibits significant plastic straining, i.e., for  $E \tan \beta / \sigma_0(1-\nu^2) > 10$  in both cases (a) and (b). In particular, the use of (28) leads to a significant underestimation of the hardness of the solid even when  $l/a = 0.05$ .<sup>3</sup> On the other hand, the new prescription (32) provides better agreement than that of relation (28) for  $l/a = 0.05$ . When  $l/a = 1$ , the curve corresponding to definition (32) follows the *FEM* solution (and the elastic curve) up to a value  $E \tan \beta / \sigma_0(1-\nu^2) \approx 10$ , but then significantly underestimates the indentation pressure for large  $E \tan \beta / \sigma_0(1-\nu^2)$  (in the indentation regime of significant plasticity). We conclude that the spherical void expansion solutions underestimate micro-hardness when

<sup>3</sup> It is important to point out that Johnson (1970) has proposed the addition of a constant term to the void expansion pressure in order to get reasonable agreement with *FEM* calculations of the indentation pressure.

significant plastic straining is present. The lack of agreement is consistent with the observation that the *FEM* indentation solution possesses markedly non-spherical contour fields of the Mises plastic strain, recall Fig. 10(b).

### 6.2. Nix and Gao approach versus *FEM* model

Nix and Gao (1998) proposed the phenomenological formula (5) to fit experimental micro-indentation curves. Eq. (5) can be re-written in terms of the contact radius  $a$  according to

$$\left(\frac{H}{H_0}\right)^2 = 1 + A\frac{l}{a}, \quad (33)$$

where  $A$  is a non-dimensional constant. This is done by noting that in the conical indentation the indentation depth  $h$  scales linearly with the actual contact radius  $a$  (Nix and Gao, 1998).

Fig. 16 shows  $(H/H_0)^2$  curves (where  $H \equiv \bar{P}_0$ ) as a function of  $l/a$  for selected values of yield strain. The normalized hardness  $H_0$  is extracted from the *FEM* calculations as the asymptotic value of  $\bar{P}_0$  in the limit  $l/a \rightarrow 0$ : the values of  $H_0$  used to the different cases are stated in Fig. 16. Predictions for a gradient solid of type  $C_1$  are included in Fig. 16(a), whereas Fig. 16(b) shows curves for a gradient solid involving only rotation gradients (case  $C_3$ ). The gradient solid  $C_1$  exhibits a nonlinear increase of  $(H/H_0)^2$  with increasing  $l/a$  (i.e. as  $a$  decreases). In contrast, the solid  $C_3$  gives a linear dependence of  $(H/H_0)^2$  upon  $l/a$ , similar to the Nix–Gao prediction. This suggests that the gradient solid of type  $C_3$  is representative of the indentation data analyzed by Nix–Gao.

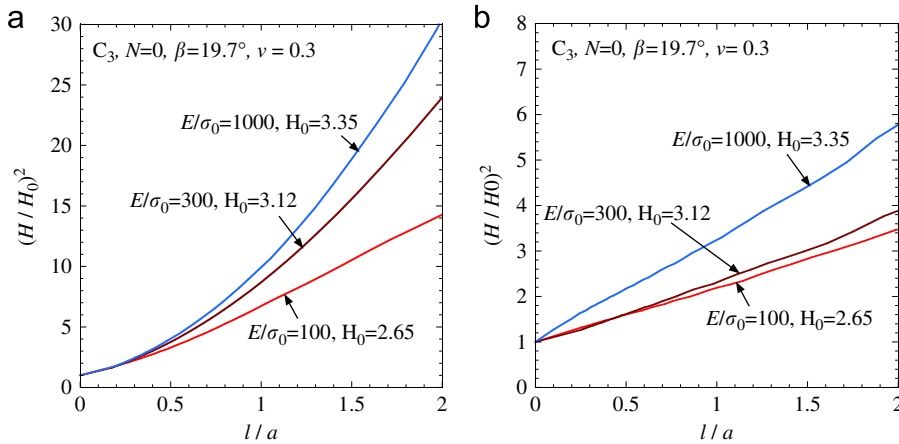
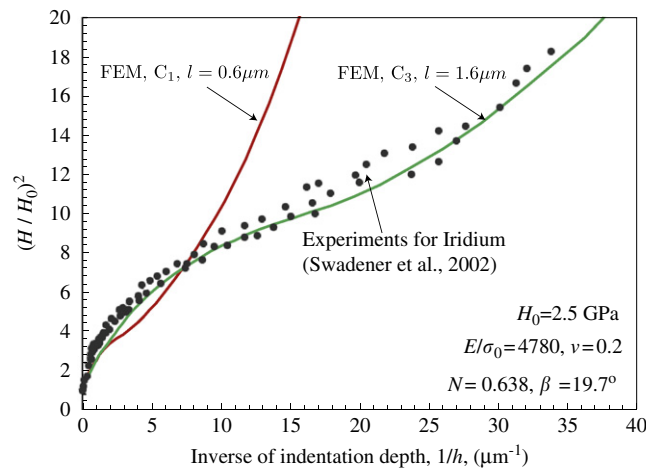


Fig. 16. The normalized square of the hardness versus the inverse of the contact radius  $l/a$  for the cases (a)  $C_1$  and (b)  $C_3$ . The predictions are plotted in this manner in order to compare with the Nix and Gao (1998) scaling relation.

### 6.3. Discussion on the Begley–Hutchinson model

There are close links between the findings of the present study and the earlier predictions by Begley and Hutchinson (1998). The Begley–Hutchinson paper assumes a different formulation of strain gradient plasticity (i.e., that of Fleck and Hutchinson, 1997), wherein the only kinematically free variable is the material displacement field, and the plastic strain field is determined at the constitutive level. Both studies explore the relative significance of stretch gradients (case  $C_2$ , closely approximated by case  $C_1$ ) and of rotation gradients (case  $C_3$ ) upon indentation size effects. While both studies explore the role of strain hardening, the present study also explores the role of yield strain upon the indentation response, and complete indentation maps are presented. Detailed comparisons are also made in the present study between the predictions of the present *FEM* model and the classical analytical ideas on indentation theory by Tabor (1948, 1951) and Johnson (1970).

In broad terms, the present study and that of Begley and Hutchinson (1998) give rather similar size effects in the practical range of indents on the micron scale. For example, it is clear from Fig. 5 of the present study, and from Fig. 6 of Begley and Hutchinson (1998) that the hardness is more sensitive to the magnitude of the length scale in case  $C_1$  than that of  $l$  in case  $C_3$  (for case  $C_3$ ,  $l = l_{CS}$  in the notation of Begley and Hutchinson, 1998). On this basis, Begley and Hutchinson conclude that the indentation test can be used to deduce the value of  $l_1$ . An alternative view is that  $l_1$  is much less than  $l_{CS}$  and indentation tests on the micron scale can be used to deduce the value of  $l_{CS}$ . The predictions given in Fig. 16 support this view, by the following argument. Assume that the observed dependence of hardness upon indent size is that noted by Poole et al. (1996) and Nix and Gao (1998), as stated in relation (33). The predictions of the present study give a similar behavior upon considering case  $C_3$  with  $l_1 = 0$  (recall Fig. 16(b)). In contrast, the case  $C_1$  gives a hardness prediction upon indent size of different qualitative shapes to that given by relation (33). A similar conclusion is drawn by making a direct



**Fig. 17.** Comparison between the present model predictions for cases  $C_1$  and  $C_3$  with the indentation hardness measurements of Swadener et al. (2002) for Iridium.

comparison between the predictions of the present study and the experimental data of Swadener et al. (2002) for Berkovich indentation of Iridium, as shown in Fig. 17. In the simulations, we have used a reference indentation hardness at large indentation depths of  $H_0=2.5$  GPa, an inverse yield strain value of  $E/\sigma_0=4780$ , a strain hardening exponent  $N=0.638$  and indenter angle  $\beta=19.7^\circ$ . The material length scale  $l$  is adjusted for the cases  $C_1$  and  $C_3$  in order to fit the model to the data at large indent depths. We find that for the  $C_1$  solid the relevant length scale is  $l=0.6\ \mu\text{m}$  and for the  $C_3$  solid it is  $l=1.6\ \mu\text{m}$ . It is clear that the solid of type  $C_3$  gives a much better correlation with the observed hardness at small indent depths.

## 7. Concluding remarks

In this work, we have investigated the micro-indentation hardness of isotropic strain gradient solids which are described by purely dissipative hardening laws. A parametric analysis of the different length scales involved in the strain gradient formulation has been carried out. It has been shown that the present strain gradient plasticity formulation provides a basis for the study of the indentation process at micron scales. In particular, the indentation contact pressure is given by the Sneddon (1948) elastic solution at extremely small indent depths and then smoothly attains the large scale indentation pressure at larger length scales. We have also shown that the length scale associated with stretch gradients,  $l_1$ , leads to strong size effects whereas rotation gradients, i.e. nonzero  $l_2$  and  $l_3$  (and  $l_1=0$ ), lead to much milder size effects.

The FEM results have been used to construct maps which give the dominant indentation mechanism as a function of (i) size of indent  $l/a$  and (ii) the strain measure  $E \tan \beta / \sigma_0 (1 - \nu^2)$ , as originally proposed by Johnson (1970). Three regimes exist: (i) elastic indentation as given by the Sneddon (1948) solution for low  $E/\sigma_0$ ; (ii) an elastic–plastic regime for solids that satisfy  $10 < E/\sigma_0 < 200$ ; and (iii) the size-dependent, rigid–plastic limit at high values of  $E/\sigma_0$ . The boundaries of these regimes are strongly affected by the choice of length scale parameters as described in Section 4.1. For example, the solid for which the strength is influenced by stretch gradients (nonzero  $l_1$ ) exhibits a large elasto–plastic regime. In contrast, the solid that has a strength influenced by rotation gradients ( $l_1=0$ ) has a rather large rigid–plastic regime.

Idiart et al. (2009) and Niordson and Hutchinson (submitted for publication) have previously noted that the present strain gradient plasticity theory predicts a decreasing Mises stress within material regions of continued plastic flow. In order to further explore this, we have provided Mises stress and effective plastic strain contour maps below the indenter. It has been confirmed that the Mises stress becomes small in regions of continued plastic flow and of large plastic gradients. This is directly attributable to the feature that the Mises stress is work-conjugate to the elastic strain, and there is a much greater penalty for elastic strain energy within the Fleck and Willis (2009b) Minimum Principle than for plastic dissipation. This feature of the tensorial strain gradient plasticity theory, as employed in this study, poses no mathematical or numerical problems, i.e. the problem remains well-posed with positive plastic work. Nonetheless, a physical interpretation of this feature remains to be established.

Our study of micro-indentation hardness has been limited to the case of gradient solids that undergo dissipative isotropic hardening. For such a class of solids, we have shown that the Tabor (1948) approximation is a useful aid to the interpretation of hardness data provided the yield strain is sufficiently low. Tabor's approximation has a broader range of applicability for the gradient solid with only rotation gradients present (i.e.  $l_1=0$ ) than for the one that involves only stretch gradients (i.e.  $l_1$  is the dominant length scale).

Finally, the present finite element strain gradient framework has been used to evaluate previous simplified indentation models at micro- and macro-scales, such as the cavity expansion solution and the Nix and Gao (1998) empirical model.

It has been found that the cavity expansion solution significantly underestimates both the micro- and macro-indentation hardness of solids particularly at low yield strains (or high values of  $E/\sigma_0$ ). This has been explained by the fact that the plastic strain fields beneath the indenter exhibit a markedly non-spherical shape and hence the hypothesis of spherically symmetric plastic strain fields is inappropriate. A comparison of the present finite element calculations with the Nix and Gao (1998) formula reveals that the gradient solid that involves only rotation gradients ( $I_1 = 0$ ) reproduces the Nix–Gao trends, i.e. the square of the indentation hardness scales linearly with the inverse of the contact radius (or equivalently with the inverse of the indentation depth).

## Acknowledgments

K.D. would like to acknowledge the support of Engineering Department, Cambridge University, while doing his postdoctoral studies.

## Appendix A. Rate-independent and rate-dependent formulations

The rate-independent and rate-dependent strain gradient plasticity theories are now contrasted. First, we discuss the rate-independent formulation, which results in a *non-local* yield function and second we present the finite element implementation of the rate-dependent formulation as used in the present work to predict indentation hardness.

The rate-independent formulation is attained in the limit of the rate sensitivity exponent  $m \rightarrow 0$  and was originally described in Fleck and Willis (2009b). Specifically, it involves two minimum principles, termed as *Minimum principle I* and *Minimum principle II* as presented below.

First, we assume that there exists a nonzero plastic strain rate field  $\dot{\epsilon}_{ij}^p$  in a sub-domain  $V_p$  of  $V$ . Since the problem is rate-independent,  $\dot{\epsilon}_{ij}^p$  in that sub-domain takes the form

$$\dot{\epsilon}_{ij}^p = \dot{\lambda} \hat{\epsilon}_{ij}^p(\mathbf{x}), \quad \dot{\lambda} \geq 0, \quad \frac{1}{V_p} \int_{V_p} \hat{\epsilon}_{ij}^p \hat{\epsilon}_{ij}^p dV = 1, \quad (34)$$

where  $\dot{\lambda}$  is the plastic multiplier and the field  $\hat{\epsilon}_{ij}^p$  serves to define a distribution of the plastic strain field. Then, following Fleck and Willis (2009b) (see Eq. (6.1) in that manuscript), one can write the minimum principle I in terms of the following functional:

$$\Phi(\sigma_{ij}^p) = \int_{S_u} t_{ij} \dot{\epsilon}_{ij}^p dS - \inf_{\hat{\epsilon}_{ij}^p} \left\{ \int_V (\sigma_y(E_p) \dot{E}_p - \sigma_{ij}^p \dot{\epsilon}_{ij}^p) dV - \int_{S_T} t_{ij} \dot{\epsilon}_{ij}^p dS \right\}. \quad (35)$$

The above expression constitutes a “*non-local*” yield function, such that yield occurs when  $\Phi = 0$ , and no yield occurs if  $\Phi < 0$ . Thus, we obtain two possible cases:

- In the case of yield, i.e.,  $\Phi = 0$ , we make use of the minimum principle II (see equation (7.1) in Fleck and Willis, 2009b). This takes the form

$$\mathcal{J} = \min_{\dot{u}_i, \dot{\lambda} \geq 0} \left\{ \int_V \frac{1}{2} [(\dot{\epsilon}_{ij} - \dot{\epsilon}_{ij}^p) L_{ijkl} (\dot{\epsilon}_{kl} - \dot{\epsilon}_{kl}^p) + h_N(E_p) \dot{E}_p] dV - \int_{S_T} [\dot{T}_i \dot{u}_i + t_{ij} \dot{\epsilon}_{ij}^p] dS \right\}, \quad (36)$$

where  $h_N(E_p) = d\sigma_y/dE_p$  denotes the hardening rate of the material. By carrying out the minimization procedure in (36), we obtain the solution for  $\dot{u}_i$  and  $\dot{\lambda}$ . Then, we have two possibilities for  $\dot{\lambda}$ : the first is  $\dot{\lambda} > 0$ , which indicates that active plastic flow occurs in the sub-domain  $V_p$ , while the second is  $\dot{\lambda} = 0$ , indicating that elastic unloading occurs from the current yield point.

- In the case of no yield, i.e.,  $\Phi < 0$ , purely elastic straining occurs and  $\dot{\epsilon}_{ij}^p = 0$  (as well as  $\dot{E}_p = 0$ ) everywhere in  $V$ . This requires the solution of the minimization problem (36), which is a standard elasticity problem.

A complete numerical implementation of the above-described rate-independent procedure is not yet fully developed, due to the nonlocal character of the yield function (35). The first steps in this direction have been taken by Niordson and Hutchinson (submitted for publication). Therefore, for convenience in the present study, we have implemented numerically the pertinent rate-dependent formulation but for a small rate sensitivity exponent ( $m = 0.1$ ) so that the corresponding indentation results are also relevant to the hardness of a rate-independent solid. Nonetheless, one should keep in mind that real materials always exhibit rate sensitivity to some degree and hence, the rate-dependent formulations are always useful.

Next, we describe the numerical implementation of the rate-dependent formulation as outlined in Section 2. The implementation employs a mixed finite element framework. In this connection, the weak form of the equilibrium equations (8) read

$$\int_V \sigma_{ij} \delta \dot{u}_{i,j} dV = \int_S T_i \delta \dot{u}_i dS, \quad (37)$$

$$\int_V q_{ij} \delta \dot{\epsilon}_{ij}^p dV + \int_V \tau_{ijk} \delta \dot{\epsilon}_{ij,k}^p dV = \int_V \sigma'_{ij} \delta \dot{\epsilon}_{ij}^p dV + \int_S t_{ij} \delta \dot{\epsilon}_{ij}^p dS, \quad (38)$$

where the plastic strain is constrained to be incompressible, i.e.  $\dot{\epsilon}_{kk}^p = 0$ .

For the finite element implementation of relations (38), we define the vector of rates of nodal degrees of freedom  $\{\dot{\mathbf{u}}^N\}$  and  $\{\dot{\boldsymbol{\epsilon}}^{pN}\}$  while  $\{\mathbf{v}\}$  and  $\{\dot{\boldsymbol{\epsilon}}^p\}$  are the vectors of components of the velocity and the plastic strain-rate at a material point within an element. In a conventional small-strain formulation, the shape functions  $[\mathbf{N}_u]$  and  $[\mathbf{N}_{ep}]$  relate  $\{\mathbf{v}\}$  and  $\{\dot{\boldsymbol{\epsilon}}^p\}$  to the corresponding nodal degrees of freedom via

$$\{\mathbf{v}\} = [\mathbf{N}_u]\{\dot{\mathbf{u}}^N\}, \quad \{\dot{\boldsymbol{\epsilon}}^p\} = [\mathbf{N}_{ep}]\{\dot{\boldsymbol{\epsilon}}^{pN}\}. \quad (39)$$

The corresponding rate of the total strain  $\{\dot{\boldsymbol{\epsilon}}\}$  and plastic strain-rate gradient  $\{\nabla\dot{\boldsymbol{\epsilon}}^p\}$  vectors are defined via the matrices  $[\mathbf{B}_u]$  and  $[\mathbf{B}_{ep}]$  according to

$$\{\dot{\boldsymbol{\epsilon}}\} = [\mathbf{B}_u]\{\dot{\mathbf{u}}^N\}, \quad \{\nabla\dot{\boldsymbol{\epsilon}}^p\} = [\mathbf{B}_{ep}]\{\dot{\boldsymbol{\epsilon}}^{pN}\}. \quad (40)$$

where the  $[\mathbf{B}]$  are the appropriate spatial derivatives of the shape functions. Using the discretized relations (39) and (40), we write the weak form of the equilibrium equations (38) as

$$\int_V [\dot{\boldsymbol{\sigma}}]^T [\mathbf{B}_u] dV \{\dot{\mathbf{u}}^N\} = \int_S [T]^T [\mathbf{N}_u] dS \{\dot{\mathbf{u}}^N\}, \quad (41)$$

$$\int_V [q]^T [\mathbf{N}_{ep}] dV \{\dot{\boldsymbol{\epsilon}}^{pN}\} + \int_V [\tau]^T [\mathbf{B}_{ep}] dV \{\dot{\boldsymbol{\epsilon}}^{pN}\} = \int_V [\sigma']^T [\mathbf{N}_{ep}] dV \{\dot{\boldsymbol{\epsilon}}^{pN}\} + \int_S [t]^T [\mathbf{N}_{ep}] dS \{\dot{\boldsymbol{\epsilon}}^{pN}\}. \quad (42)$$

Plastic incompressibility is a linear equality constraint on  $\{\dot{\boldsymbol{\epsilon}}^{pN}\}$  and can be imposed in a rather straightforward manner as detailed in Cook et al. (1974, Chapter 9) and is not detailed here. The solution of the above two simultaneous equilibrium equations is done via an iterative scheme wherein each equation is solved independently via a Newton scheme and convergence then checked for the two equations together.

## Appendix B. Sensitivity of hardness to the choice of boundary conditions at the contact

The sensitivity of indentation pressure to the choice of higher order boundary conditions at the contact area is now investigated. More specifically, we either apply zero higher order tractions  $t_{ij} = 0$  at the contact area or a zero plastic strain-rate  $\dot{\epsilon}_{ij}^p = 0$ . According to Wei and Hutchinson (2003), these two different boundary conditions do not significantly affect the predicted contact pressure at the indenter. To confirm this, we carried out two indentation simulations; in the first  $t_{ij} = 0$  at the contact area while in the second  $\dot{\epsilon}_{ij}^p = 0$  at the contact area. Fig. 18 confirms the findings of Wei and Hutchinson (2003): the difference between the responses for  $\dot{\epsilon}_{ij}^p = 0$  and the  $t_{ij} = 0$  is on the order of 5% at  $l/a < 0.3$ , and becomes negligible at  $l/a > 0.3$ .

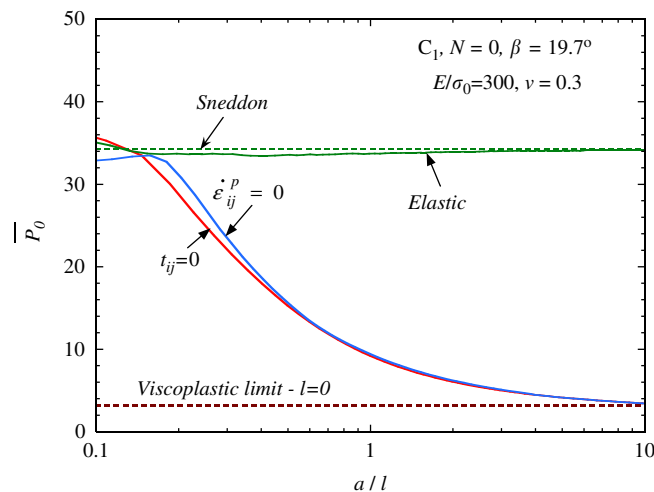


**Fig. 18.** Normalized contact pressure versus the normalized contact radius as predicted by a purely elastic solid and a strain-gradient solid of type  $C_1$ . Predictions of two boundary conditions (BCs) in the contact are compared: (i) the BC used in the bulk of the study  $t_{ij} = 0$  and (ii)  $\dot{\epsilon}_{ij}^p = 0$  imposed on the contact surface.

## References

- Ashby, M.F., 1970. The deformation of plastically non-homogeneous materials. *Philos. Mag.* 21, 399–424.  
 Balint, D.S., Deshpande, V.S., Needleman, A., Van der Giessen, E., 2006. Discrete dislocation plasticity analysis of the wedge indentation of films. *J. Mech. Phys. Solids* 54, 2281–2303.  
 Begley, M.R., Hutchinson, J.W., 1998. The mechanics of size-dependent indentation. *J. Mech. Phys. Solids* 46, 2049–2068.  
 Borg, U., 2007. Strain gradient crystal plasticity effects on flow localization. *Int. J. Plasticity* 23 (8), 1400–1416.

- Bower, A.F., Fleck, N.A., Needleman, A., Ogbonna, N., 1993. Indentation of a power law creeping solid. *Proc. R. Soc. Lond. A* 441, 97–124.
- Cook, R.D., Malkus, D.S., Plesha, M.E., 1974. *Concepts and Applications of Finite Element Analysis*. John Wiley and Sons, Inc.
- Danas, K., Deshpande, V.S., Fleck, N.A., 2010. The role of surface coatings in size effects: discrete dislocations vs. strain-gradient crystal plasticity. *Int. J. Plasticity* 26, 1792–1805.
- Deshpande, V.S., Needleman, A., Van der Giessen, E., 2005. Plasticity size effects in tension and compression of single crystals. *J. Mech. Phys. Solids* 49, 2661–2691.
- Evans, A.G., Hutchinson, J.W., 2009. A critical assessment of theories of strain gradient plasticity. *Acta Mater.* 57, 1675–1688.
- Fleck, N.A., Hutchinson, J.W., 1997. Strain gradient plasticity. In: Hutchinson, J.W., Wu, T.Y. (Eds.), *Advances in Applied Mechanics*, vol. 33. Academic Press, New York, pp. 295–361.
- Fleck, N.A., Hutchinson, J.W., 2001. A reformulation of strain gradient plasticity. *J. Mech. Phys. Solids* 49, 2245–2271.
- Fleck, N.A., Muller, G.M., Ashby, M.F., Hutchinson, J.W., 1994. Strain gradient plasticity: theory and experiment. *Acta Metall. Mater.* 42, 475–487.
- Fleck, N.A., Willis, J.R., 2009a. A mathematical basis for strain gradient plasticity theory. Part I: scalar plastic multiplier. *J. Mech. Phys. Solids* 57, 161–177.
- Fleck, N.A., Willis, J.R., 2009b. A mathematical basis for strain gradient plasticity theory. Part II: tensorial plastic multiplier. *J. Mech. Phys. Solids* 57, 1045–1057.
- Forest, S., Barbe, F., Cailletaud, G., 2000. Cosserat modelling of size effects in the mechanical behaviour of polycrystals and multi-phase materials. *Int. J. Solids Struct.* 37, 7105–7126.
- Gudmundson, P., 2004. A unified treatment of strain gradient plasticity. *J. Mech. Phys. Solids* 52, 1379–1406.
- Gurtin, M.E., 2002. A gradient theory of single-crystal viscoplasticity that accounts for geometrically necessary dislocations. *J. Mech. Phys. Solids* 50, 5–32.
- Gurtin, M.E., Anand, L., 2005. A theory of strain-gradient plasticity for isotropic, plastically irrotational materials. Part I: small deformations. *J. Mech. Phys. Solids* 53, 1624–1649.
- Hwang, K.C., Jiang, H., Huang, Y., Gao, H., Hu, N., 2002. A finite deformation theory of strain gradient plasticity. *J. Mech. Phys. Solids* 50, 81–99.
- Hill, R., 1950. *Theory of Plasticity*. Oxford University Press.
- Hutchinson, J.W., 2000. Plasticity at the micron scale. *Int. J. Solids Struct.* 37, 225–238.
- Idiart, M.I., Deshpande, V.S., Fleck, N.A., Willis, J.R., 2009. Size effects in the bending of thin foils. *Int. J. Eng. Sci.* 47, 1251–1264.
- Johnson, K.L., 1970. The correlation of indentation experiments. *J. Mech. Phys. Solids* 19, 115–126.
- Johnson, K.L., 1985. *Contact Mechanics*. Cambridge University Press.
- Komaragiri, U., Agnew, S.R., Gangloff, R.P., Begley, M.R., 2008. The role of macroscopic hardening and individual length-scales on crack tip stress elevation from phenomenological strain gradient plasticity. *J. Mech. Phys. Solids* 56, 3527–3540.
- Kubin, L.P., Canova, G., Condat, M., Devincere, B., Pontikis, V., Bréchet, Y., 1992. Dislocation microstructures and plastic flow: a 3D simulation. *Solid State Phenom.* 23–24, 455–472.
- Nachum, S., Fleck, N.A., Ashby, M.F., Colella, A., Matteazzi, P., 2010. The microstructural basis for the mechanical properties and electrical resistivity of nanocrystalline Cu-Al<sub>2</sub>O<sub>3</sub>. *Mater. Sci. Eng. A* 527, 5065–5071.
- Niordson, C.F., Hutchinson, J.W. Basic strain gradient plasticity theories with application to constrained film deformation. *J. Mech. Mater. Struct.* 6, 395–416.
- Nix, W.D., Gao, H., 1998. Indentation size effects in crystalline materials: a law for strain gradient plasticity. *J. Mech. Phys. Solids* 46, 411–425.
- Oliver, W.C., Pharr, G.M., 1992. An improved technique for determining hardness and elastic modulus by load and displacement sensing indentation experiments. *J. Mater. Res.* 7, 1564–1583.
- Pethica, J.B., Hutchings, R., Oliver, W.C., 1983. Hardness measurements at penetration depths as small as 20 nm. *Philos. Mag.* A48, 593–606.
- Pharr, G.M., Herbert, E.G., Gao, Y., 2010. The indentation size effect: a critical examination of experimental observations and mechanistic interpretations. *Annu. Rev. Mater. Res.* 40, 271–292.
- Poole, W.J., Ashby, M.F., Fleck, N.A., 1996. Microhardness of annealed and work-hardened copper polycrystals. *Scr. Mater.* 34, 559–564.
- Smyshlyaev, V.P., Fleck, N.A., 1996. The role of strain gradients in the grain size effect of polycrystals. *J. Mech. Phys. Solids* 44, 465–495.
- Sneddon, I.N., 1948. Boussinesq's problem for a rigid cone. *Proc. Cambridge Philos. Soc.* 44, 492.
- Stelmashenko, N.A., Brown, L.M., 1996. Deformation structure of microindentations in W(100): a transmission electron microscopy study. *Philos. Mag. A* 74(5), 1195–1206.
- Stelmashenko, N.A., Walls, M.G., Brown, L.M., Milman, Y.V., 1993. Microindentations on W and Mo oriented single crystals: an STM study. *Acta Metall. Mater.* 41, 2855–2865.
- Swadener, J.G., George, E.P., Pharr, G.M., 2002. The correlation of the indentation size effect measured with indenters of various shapes. *J. Mech. Phys. Solids* 50, 681–694.
- Tabor, D., 1948. A simple theory of static and dynamic hardness. *Proc. R. Soc. Lond. A* 192, 247–274.
- Tabor, D., 1951. *Hardness of Metals*. Clarendon Press, Oxford.
- Van der Giessen, E., Needleman, A., 1995. Discrete dislocation plasticity: a simple planar model. *Model. Simul. Mater. Sci. Eng.* 3, 689–735.
- Wei, Y., Hutchinson, J.W., 2003. Hardness trends in micron scale indentation. *J. Mech. Phys. Solids* 51, 2037–2056.